Chapter 4

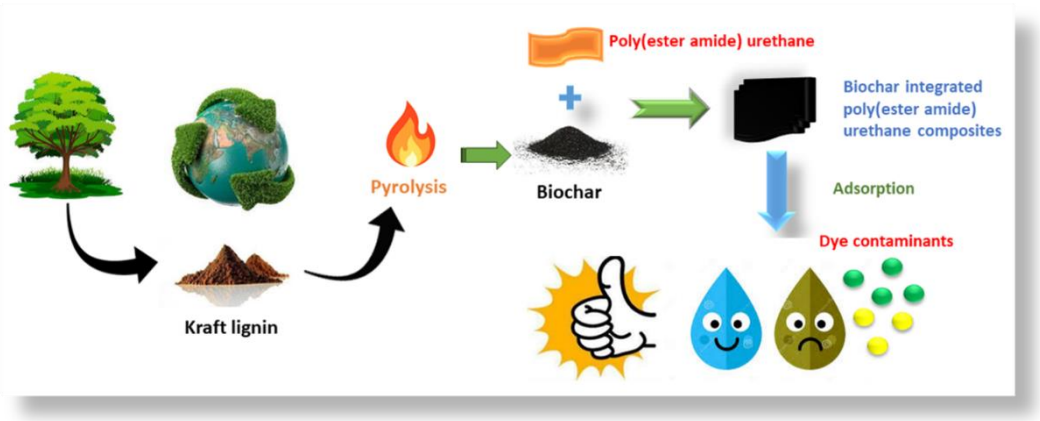
Poly(ester amide) urethane
Biochar integrated poly(ester amide) urethane composites
Pyrolysis
Biochar
Adsorption
Dye contaminants
Kraft lignin

Lignin derived biochar/ poly(ester amide urethane) nanocomposites

Highlights

The pursuit of incorporating eco-friendly reinforcing agents in polymer composites has accentuated the exploration of various natural biomass-derived materials. Biochar has emerged as a focal point for its potential to replace other traditional inorganic mineral reinforcing agents. In this work, we navigate through the fabrication of biochar from kraft lignin, followed by integration into poly(ester amide urethane) matrix in varying amounts to prepare the polymer nanocomposites by a feasible method. The structural evaluation of these nanocomposites was accomplished by different instrumental methods, viz., FTIR, XPS, PXRD, etc. Moreover, these polymer nanocomposites exhibited superior mechanical properties with an increment in tensile strength factor by 45% in comparison to its pristine matrix, along with an excellent toughness value of 90.22 MJm^{-3} at a low loading amount of only 1 wt%. Additionally, these composites showcased excellent improvement in thermal properties with a sharp rise in the T_g value from -28.15 to 84 °C, while also championing sustainability through inherent biodegradability attributes. Beyond their structural prowess, these polymer nanocomposites demonstrated excellent potential as adsorbents, displaying efficient removal of malachite green and tartrazine dyes from aqueous systems with a removal efficiency of 87.25% and 73.98%, respectively. An extensive kinetics study revealed the pseudo second order model to be the precision tool to assess the dye removal study. Complementing this, the Langmuir adsorption isotherm provided a framework to assess the sorption features of the polymer nanocomposites. Overall, these biochar integrated polymer matrices boast remarkable recovery capabilities up to seven cycles of usage, thereby defining sustainability as well as economic feasibility.

Parts of this chapter are ready to be communicated as

Kar, A., and Karak, N. Lignin-based biochar/poly(ester amide urethane) nanocomposites: Sustainable approach for dye removal from contaminated wastewater.

4.1. Introduction

Over the past couple of years, the rapid rate of depletion of fossil fuel reserves and alarming environmental safety have become the focal point of concern for researchers across the globe as vividly discussed in **Chapter 1**. In this milieu, there has been an unprecedented growth in pursuit of sustainable manufacturing processes [1]. The exploration of various biocomposites along with fabrication of new environmentally sustainable materials extracted from various waste and renewable substances have captured a lot of attention among the scientific community worldwide. Under this pretext, biochar proved to be a great alternative to other conventional carbon fillers such as graphene, carbon nanotubes, etc. owing to its low cost, sustainability and a range of other desirable features as enumerated in **Chapter 1** [2, 3]. This surge in interest on biochar stems from its potential to address pressing environmental as well as economic challenges.

Biochar is defined as a carbonaceous material produced by slow pyrolysis of the carbon-rich biomass at a high temperature ranging from 300-900 °C in the absence or even at the presence of a limited supply of oxygen [4]. Notably, a broad spectrum of carbon-rich organic substances can serve as a viable source for biochar precursors inclusive of agricultural biomass obtained from plant or animal sources, lignocellulose biomass, activated sludge, municipal or industrial wastes, etc. [5-7] This entire process of carbonization leads to loss of carbon content from the solid phase due to release of volatiles from feedstock into the atmosphere. Consequently, the carbonization method is considered as a pivotal parameter to assess the yield and quality of biochar [8]. Overall, this process of slow pyrolysis and the diverse range of materials that can be utilized as biochar precursors underscore the significance of careful assessment and selection in the creation of high-quality biochar products.

Synthetic pigments as well as dyes act as a formidable source for carrying out environmental degradation, with their continuous pervasive utility expanding across various genres, inclusive of plastics manufacturing, textiles, leather processing, paper production, etc. The effluents discharged by these industrial sectors carry extensive loads of intractable toxic by-products and suspended organic materials, thus posing a substantial threat to our environment. It is further estimated that out of the huge array of commercially available pigments and dyes, more than ten thousand are currently in active deployment, therefore collectively culminating in production of approximately 0.7 million metric tons

of effluents as well as by-products, emanating from dye production. Within this broad spectrum of pigments and dyes, two important conspicuous examples come to the fore, viz., malachite green and tartrazine. Malachite green is a well-known synthetic dye, and it boasts extensive utility in textile, cosmetics, plastic and paper industries. On the other hand, tartrazine, also known as Yellow 5, finds widespread applications in textiles as well as in food and beverage industries. Malachite green garners widespread speculation on ground of its various detrimental attributes, viz., acute toxicity, genotoxicity, cytotoxicity, neurotoxic potential, dermal irritations, etc. on exposure to various living organisms especially aquatic species. In turn, certain by-products of malachite green also bear the mantle of xenobiotic and carcinogenic nature. This has subsequently raised significant health and environmental implications. On the other hand, tartrazine has been found to inflict a gamut of adverse health implications on human beings on direct exposure which are inclusive of carcinogenicity and allergenicity in higher concentrations. In response to these critical environmental challenges, the scientific community has been strictly galvanized to carry out exploration of various efficient remedies [6-8]. Several conventional technologies, viz., reverse osmosis, chromatography, chemical oxidation, etc. have been enlisted in carrying out decolorization of dye-containing wastewater. However, these approaches are marred by significant limitations, encompassing prohibitive costs, incomplete dye removal and exorbitant energy demands, thereby hampering their viability. Currently, adsorption, with the deployment of biochar or modified activated biomass, reigns supreme as the most efficacious methodology for purging pollutants from aqueous phases, driven by their cost-effective and eco-friendly nature.

As per a recent survey conducted by Scopus in 2020, it has been found that the utilization of this material has seen a notable increase over the last few years owing to its cost-effectiveness and other beneficial properties viz., presence of greater number of oxygen containing functional moieties, large surface area, high cation exchange capacity, etc. [9] Due to the presence of these aforementioned traits, biochar has found its application in diverse domains viz., as adsorbents in wastewater treatment for removal of organic dyes, trace metals, VOCs, pesticides, polycyclic aromatic hydrocarbons. etc. The sorption feature of biochar can be attributed to the presence of valence sheets which are disordered in nature and result in formation of a large number of active sites from unpaired electrons as well as incomplete saturated valence sites [10]. Moreover, presence of delocalized π

electrons and different oxygen containing functional groups facilitate the phenomenon of adsorption via various forces of interaction, viz., hydrogen bonding, acid-base interactions, etc. All these traits collectively are conducive enough to make biochar a promising alternative to activated carbon in the field of adsorption.

Over contemporary years, there has been an escalating demand for smart materials in the market domain. In this regard, polymer composites have occupied a foremost position owing to their easy processing technique, low cost and light weight nature. Biochar, being a sustainable, low-cost and environmentally benign material has been used as a reinforcing agent in order to improve the properties of the pristine polymers over other conventional carbon additives. Studies revealed that biochar reinforced polymer composites are known to exhibit better thermal, mechanical as well as electrical conductivity properties [11]. These composites are widely used nowadays in manifold genres viz., packaging, automobiles, aerospace industries, etc. Unlike other carbon fillers, the properties of biochar can be easily tuned by altering the pyrolysis temperature conditions in order to improve the hydrophobicity feature which in turn facilitates better compatibility with polymer matrices [12].

Therefore, in this context, biochar was prepared from commercial Kraft lignin via pyrolysis process. Lignin is considered as an appealing feedstock for carbonization purpose owing to its facile availability, low cost and renewability. Herein, an attempt has been made to convert lignin into a high-grade adsorbent material by carrying out pyrolysis at a high temperature. In turn, the synthesized biochar was employed as a reinforcing agent for carrying out incorporation in the polymer matrix. The latter was prepared by invoking a melt polycondensation technique via an environmentally benign route [13]. The biochar-poly(ester amide urethane) nanocomposites were fabricated by altering the weight percentages of biochar material inside the polymer matrix. All the synthesized polymer composites along with the biochar material underwent comprehensive evaluation and different tests were carried out. These assessments aimed to instill specific properties deemed advantageous for applications across diverse domains.

4.2. Experimental

4.2.1. Materials

A variety of chemicals, including glycerol anhydrous, citric acid anhydrous, hexamethylene diamine, KOH, PVA, NaOH, oxalic acid, and *p*-TSA were utilized. The specifications for these chemicals were consistent with those discussed in **Chapter 2** elaborately. IPDI, hexane, HCl, ethanol and DMSO were also used as mentioned in **Chapter 3** with complete specifications. The bacteria strain, viz., *Bacillus subtilis* was used for conducting the biodegradation study as indicated in **Chapter 2**.

Kraft lignin was procured from Sigma Aldrich, USA. It typically appears as a dark brown powder with a characteristic woody odour. It bears a density value of 1.2-1.3 g/cm^3. It is generally insoluble in water but is highly soluble in some organic solvents, viz., DMSO as well as dimethylformamide (DMF). Being an amorphous compound, it does not have a distinct melting point and gets eventually softened and decomposed upon heating. The molecular weight of the compound is found to be quite high, which contributes significantly to its complex amorphous structural entity.

Phosphoric acid was obtained from Rankem, India. It is an odourless and colourless syrupy liquid. It bears a molecular weight of 97.99 g/mol with a density value of 1.68 g/cm^3. Since it is liquid at room temperature, it does not possess a distinct melting point. It bears a boiling point of approximately 158 °C. It has higher level of purity ranging from 99.5% to 99.9%.

Malachite green oxalate was procured from SRL, India. It is a chemical compound that has been used as a dye with a molecular weight of approximately 454.91 g/mol. It appears as a crystalline solid bearing green color with a high level of purity. It is sparingly soluble in water and has greater solubility in methanol as well as ethanol.

Tartrazine was obtained from SRL, India. It is a synthetic compound bearing yellow or lemon-yellow color with molecular weight of approximately 534.37 g/mol. It is a water-soluble dye and its solubility in water confers its utility in different food products as food additives.

4.2.2. Methods

4.2.2.1. Synthesis of biochar

Biochar material was synthesized from kraft lignin, and the preparation involved multiple steps as discussed below. Initially, the kraft lignin powder was thoroughly rinsed with deionized water to get rid of any sort of contaminants or undue residues. Subsequently, the kraft lignin powder was subjected to drying at room temperature for an entire day followed by drying in a convection oven at 100 °C for five hours. This was further followed by suspending the kraft lignin powder in 30 mL of 30 wt/wt% of ortho phosphoric acid solution which served as an activating agent. The entire contents of the prepared solution was subjected to uniform suspension for an entire day followed by carrying out drying at 100 °C which resulted in the formation of an imbued mixture. Furthermore, the impregnated mixture was allowed to undergo carbonisation at 450 °C in a muffle furnace for a time duration of 1.5 h. Subsequent to accomplishment of the carbonisation procedure, the sample was ground uniformly to a fine mixture, washed and eventually filtered using a funnel. The solid contents were then washed off with 200 mL of 0.1 M HCl solution in order to get rid of any unwanted residues or chemicals. This step was then followed by washing the solid portion with distilled water until the pH of the filtrate dropped down to 7 (neutral state). Subsequently, the washed product was subjected to drying for a time regime of 24 h at 100 °C [14]. The obtained product was then then utilized as filler for carrying out fabrication of polymer composites.

4.2.2.2. Preparation of biochar/poly(ester amide urethane) nanocomposite

Synthesis of the polymer nanocomposites involved incorporation of the biochar material into the polymer matrix via an *in-situ* strategy. Herein, the polymeric material, i.e. poly(ester amide) resin was synthesized by carrying out melt polycondensation between the primary substrates, viz. hexamethylene diamine, citric acid, and glycerol via a one pot reaction as mentioned in our previous report. The contents of the reaction mixture were heated continuously at 140 °C for a time period of three hours under vacuum conditions. This was followed by collection of the end product as a thick viscous matter before attaining the gelation point by carrying out close monitoring of the course of the reaction till its completion. In turn, an attempt was made to upgrade the strength as well as texture of the polymeric material by incorporating PVA into the matrix in DMSO solvent. The reaction mixture was further subjected to constant heating at 80 °C for 1 h until accomplishment of a consistent mixture. This was followed up by the addition of biochar particles dispersed in 1 mL of DMSO solvent. Subsequently, the reaction was conducted

for another 45 minutes followed by addition of isophorone diisocyanate in a dropwise pattern [15]. Moreover, the entire process was continued for another 30 minutes at 60 °C until absolute consumption of isocyanate was attained under the stated preceding reaction parameters. The entire process of synthesis of biochar along with fabrication of the polymer nanocomposites is illustrated in **Scheme 4.1.**

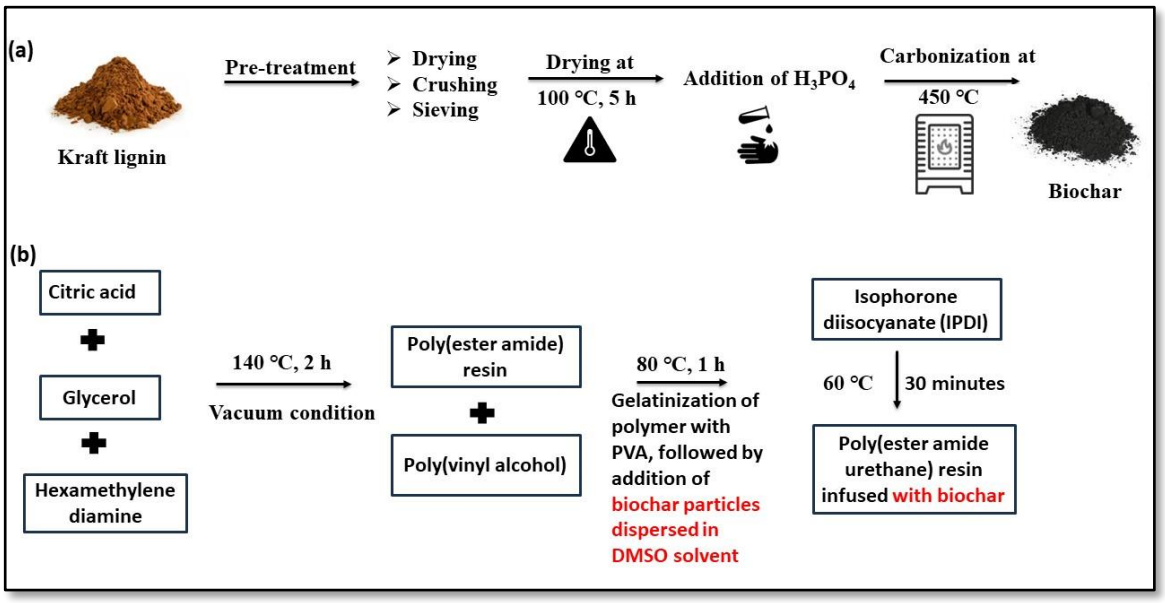

Scheme 4.1. Scheme for **(a)** synthesis of biochar, and **(b)** fabrication of biochar integrated poly(ester amide urethane) nanocomposites.

After completion of the reaction, the polymeric contents were sonicated in an ultra-bath sonicator for a time period of 20 minutes in order to agitate the biochar particles as well as to achieve uniform dispersion in the overall reaction mixture. Following this, the contents of the reaction mixture were poured down into Teflon sheets and were subjected to drying at 50 °C in a conventional drying oven for two to three days followed by drying at a slightly high temperature, i.e., 70 °C for another four to five days until they attain their touch-free condition. In due course, the polymeric films were taken out from the hot-air oven and were employed to carry out different analyses.

As mentioned earlier, three biochar/poly(ester amide urethane) nanocomposites were fabricated at different weight percentages of biochar. Under this context, they were assigned correspondingly as BCNC 0.1, BCNC 0.5 and BCNC 1.0 as depicted in **Table 4.1.**

Table 4.1. Various compositions of IPDI, PVA, BC, and poly(ester amide) resin.

Sample code	Poly(ester amide) resin (g)	PVA (g)	IPDI (g)	BC (wt%)
BCNC 0.1	1	0.6	0.2	0.1
BCNC 0.5	1	0.6	0.2	0.5
BCNC 1.0	1	0.6	0.2	1.0

4.2.3. Characterization

4.2.3.1. Structural analysis

The synthesized biochar material and biochar/ poly(ester amide urethane) nanocomposites bearing various loadings of biochar material underwent extensive characterization using various spectroscopic and analytical techniques inclusive of FTIR spectroscopy, XPS, PXRD, Raman study, BET analysis, proximate analysis, SEM-EDX, TEM as well as FESEM study. The details of instrumentation for FTIR spectroscopy have already been elaborately discussed in **Chapter 2**. Similarly, minute details of instrumentation for XPS and PXRD analyses have been explicitly enumerated in **Chapter 3.** In turn, Raman analysis was conducted in a Raman spectrometer (Renishaw, Germany) having series number 514 Laser. Elemental analyses were conducted in a CHNS analyzer (Thermoscientific) having the model number Flash 2000. Additionally, the surface area and pore analysis of biochar material was conducted in a Brunauer-Emmett-Teller (BET) pore and surface area analyzer (Quantachrome, NOVA 1000E). Proximate analysis of biochar was carried out in a muffle furnace (LabTech, STM, 1200 series) as per ASTM standards D5142. Transmission electron microscopy (TEM, FEI manufacturer, USA, G220, TECHNAI) analysis was conducted to characterize the biochar particles as well as assess the particle size distribution in the biochar/polymer dispersion. The topographical information of biochar material as well as the nanocomposite was recorded in a field emission scanning electron microscopy instrument (FESEM) holding model number JSM-7200F. Scanning electron microscopy coupled with energy dispersive X-ray spectroscopy (SEM-EDX, JEO, JSM-6390 LV, Japan) technique was utilized to assess the surface morphology along with the elemental composition of biochar material and its nanocomposite. All other methodologies and instrumentation utilized to assess the

performance characteristics, viz., mechanical, thermal, and biodegradation were meticulously discussed in **Chapter 2**.

4.2.3.2. Dye adsorption study

In order to conduct the dye adsorption study of biochar and biochar-reinforced poly(ester amide urethane) nanocomposite, adsorption capacities were evaluated for two different dyes, viz., malachite green (cationic dye) and tartrazine (anionic dye). Since both the dyes are soluble in water, stock solutions with concentration of 1000 mg/L were prepared followed by preparation of solutions of other lower concentrations by carrying out necessary dilutions. To invoke the effect of adsorption capacity, 30 mg of biochar as well as biochar-reinforced polymer nanocomposites were added to 50 mL of 50 ppm dye solutions. Subsequently, batch adsorption studies were carried forward by choosing the optimal composition of the nanocomposite material as the representative sample material.

Different tests were performed by taking adsorbent dosages of 5-40 mg of biochar as well as nanocomposite materials in 50 mL of dye solutions with concentrations varying from 10-60 ppm along with pH values ranging from 2-12. Meanwhile, the pH parameters were adjusted using 0.1 N NaOH and HCl solutions. All the solutions were stirred consistently using a magnetic bead stirrer at 540 rpm. After execution of the tests, the adsorbent materials were separated by conducting filtration and the dye concentration before and after uptake of the dye materials were measured by using a UV-visible spectrophotometer. In turn, variables, viz., adsorption (%) or removal efficiency (%) and adsorption capacity (q_e, mg/g) were estimated invoking equations **4.1.** and **4.2.**, respectively [16-18].

$$\text{Removal efficiency (\%)} = \frac{C_0 - C_e}{C_0} \times 100 \qquad \textbf{4.1.}$$

$$\text{Adsorption capacity } (q_e) = \frac{(C_0 - C_e)V}{m} \qquad \textbf{4.2.}$$

where C_o refers to the initial concentrations of dye solution (in ppm) and C_e denotes concentration of dye solution after attaining adsorption equilibrium (in ppm), V signifies volume of the dye solution (in mL) and m refers to the adsorbent mass (biochar and its nanocomposite material) used in running the experiment (in g), respectively.

4.2.3.3. Assessment of kinetics study

In order to scrutinize the adsorption mechanism, 30 mg of biochar and biochar-reinforced poly(ester amide urethane) material were added to 50 mL of dye solutions (both malachite green and tartrazine solutions) taken into consideration. The dye solutions were stirred uniformly using magnetic bead stirrers for various intervals of time (10-120 mins). After elapse of pre-determined time span, amount of dye solutions remaining in the containers were taken out, collected in separate vials and eventually measured using a UV-visible spectrophotometer. Under this context, pseudo-first order (PFO), pseudo-second order (PSO) and intra particle diffusion (IPD) models were explored to perceive the adsorption kinetics of dye solutions on biochar/biochar-reinforced nanocomposite materials [19, 20].

4.2.3.3.1. PFO model

This model is significant in addressing the adsorption kinetics on the pretext that the availability of vacant sites on the surface of the adsorbent material is directly proportional or linked to the occupancy of the available binding regions. The linear form of PSO model is delineated as-

$$\log(Q_e - Q_t) = \log Q_e - \frac{k_1 t}{2{\cdot}303} \qquad \textbf{4.3.}$$

where Q_e and Q_t denote the adsorption capacities or amount of dye material removed after attaining equilibrium state and variable time interval, t, respectively. The term k_1 denotes the rate constant in min^{-1} for this kinetic model. In turn, a linear plot of log (Q_e – Q_t) vs time provides the values for k_1 and Q_e from the slope and intercept terms, respectively.

4.2.3.3.2. PSO model

This model is pertinent in explaining the adsorption mechanism on the ground that the rate of occupancy of vacant adsorption sites is directly proportional or linked to the square of the number of unoccupied binding zones of the adsorbent molecules. The model is generally denoted as-

$$\frac{t}{Q_t} = \frac{1}{k_2 Q_e^2} + \frac{t}{Q_e} \qquad \textbf{4.4.}$$

where Q_e and Q_t refer to the adsorption capacities or amount of dye material removed after attaining equilibrium state and variable time interval, t, respectively. The term k_2 signifies the rate constant in $gmg^{-1}min^{-1}$ for this kinetic model. Moreover, plot of t/Q_t vs time produces the values for k_2 and Q_e from the intercept and slope terms, respectively.

4.2.3.3.3. IPD model

This model highlights an overall external transfer of mass as well as rate determining or controlling mechanistic step. The model is generally depicted as-

$$Q_t = k_{ip}t^{0.5} + c \qquad \textbf{4.5.}$$

where Q_t refer to the adsorption capacity of dye material at time t and k_{ip} depicts the rate constant in mg g^{-1} $min^{-1/2}$ for this kinetic model. In turn, plot of Q_t vs $t^{0.5}$ produces a linear correlation between the two parameters. In turn, c (mg g^{-1}) refers to the intercept and the value of the rate constant can be assessed easily from the slope of line of regression.

4.2.3.4. Assessment of isotherm study

Batch experiments were performed to evaluate the adsorption isotherms of the dye solutions on biochar/biochar-reinforced nanocomposite materials. Herein, 30 mg of adsorbent materials were added to 50 mL of dye solutions. Meanwhile, the dye solutions along with their respective were varied from 10 to 60 ppm. Subsequently, the reaction was allowed to run for a time duration of 40 minutes. After the prescribed time period, the concentrations of the residual dye solutions were measured using a UV-visible spectrophotometer. Additionally, the acquisitioned equilibrium data procured from adsorption assessments were applied to fit into the Freundlich, Langmuir and Temkin isotherm models which are denoted in equations **4.6.**, **4.7.** and **4.8.**, respectively [20-22].

4.2.3.4.1. Freundlich isotherm model

This model accounts for multilayer adsorption on different heterogeneous surfaces or sites. The mathematical expression of this empirical model is depicted below-

$$\log Q_e = \log k_f + \frac{1}{n}\log C_e \qquad \textbf{4.6.}$$

where C_e and Q_e refer to the concentration and adsorption capacity of the dye solutions after achieving equilibrium state. The term k_f signifies the Freundlich constant or the distribution coefficient whereas n stands for correction factor. The linearized version of this empirical model provides value for slope which is equivalent to 1/n and intercept stands out to be log C_e.

4.2.3.4.2. Langmuir isotherm model

This model demonstrates monolayer adsorption on various homogeneous sites or surfaces with no lateral or edgewise interactions with the adsorbed moieties followed by involvement of persistent amount of adsorption energies. The mathematical expression of this empirical model is depicted below-

$$\frac{C_e}{Q_e} = \frac{Ce}{Q_m} + \frac{1}{Q_m k_L} \quad \textbf{4.7.}$$

where Q_e stands for adsorption capacity or quantity of dye removed per g of biochar/biochar-reinforced nanocomposite material after attaining equilibrium state. The term Q_m signifies the maximum amount of dye molecules undergoing adsorption phenomenon per g of adsorbent species. C_e denotes the concentration of dye solutions after achieving equilibrium position, whereas k_L refers to the Langmuir constant. The linearized plot of equation **4.7.** provides value for slope which is equivalent to 1/Qm and intercept equals out to be 1/ Qmk_L.

4.2.3.4.3. Temkin isotherm model

This model manifests the interaction of adsorbate as well as adsorbent interactions especially taking into consideration the bonding energy. However, this model negates very large and very small values of concentration. This empirical model takes into presumption multi-layer adsorption process along with linear reduction in the amount of heat or energy of adsorption. The mathematical form of this model is expressed below-

$$Q_e = \frac{RT}{b} ln\, c_e + \frac{RT}{b} ln\, k_m \quad \textbf{4.8.}$$

where R stands for universal gas constant in $Jmol^{-1}K^{-1}$ and Q_e stands for adsorption capacity or quantity of dye removed per g of biochar/biochar-reinforced nanocomposite

material after attaining equilibrium state. C_e denotes the concentration of dye solutions after achieving equilibrium position, whereas k_m refers to the Temkin isotherm constant in Lg^{-1}. Herein, b denotes Temkin constant (or heat of sorption) in $Jmol^{-1}$and T refers to absolute temperature in Kelvin. The linearized plot of equation **4.8.** provides value for slope which is equivalent to RT/b and intercept equals out to be $1/ Q_m k_L$.

4.2.3.5. Desorption and reusability tests

This test is perceived as a vital tool to gauge the feasibility of the material. In this adsorption/desorption test, initially 30 mg of biochar was subjected to 50 mL of dye solution bearing concentration of 50 ppm. The experiment was allowed to run for a time period of 40 minutes with uniform stirring speed maintained at 200 rpm. The amount of dye adsorbed by the adsorbent material was recorded and studied explicitly with the help of a UV-visible spectrophotometer. Afterwards, the desorption test was conducted by extracting out the solution with the help of a syringe and was restored with 20 mL of absolute ethanol. The reaction was run for another 30 minutes followed by drying the adsorbent at 100 ℃ for an hour along with removal of absolute ethanol. Subsequently, the weight of the regenerated adsorbent material was recorded in order to assess amount of weight loss. Additionally, the regenerated adsorbent was further utilized to carry out dye adsorption study as described above. The adsorption/desorption test was conducted successively for seven cycles [23, 24].

4.3. Results and discussion

4.3.1. Synthesis of biochar

The preparation of biochar involves carbonization of the Kraft lignin powder at an elevated temperature for a finite time span. From a chemical perspective, the entire process of decomposition of Kraft lignin commences with the breakdown of different weaker bonds which are inclusive of C-OH as well as hydrogen bonds. With further increment in temperature, different robust bonds, viz., β-O-4 linkages are eventually broken down. Under this context, in the initial low temperature phase of pyrolysis process, there is formation of different compounds, viz., styrene, toluene, aldehydes, guaicyl hydroxyl entities, etc. Subsequently, in the higher temperature phase of pyrolysis procedure, catechols, p-hydroxy phenols as well as cresols are produced. The rupture of β-O-4 linkages generates free radicals which facilitate the depolymerization of lignin process.

These free radicals can further combine to generate different substances such as 2-methoxy-4 methylphenol, etc. [25, 26]. It was observed that at higher temperatures, generally above 300 °C, random repolymerization of these free radicals results in the formation of the biochar material. Moreover, the fabrication procedure of biochar invoked the usage of phosphoric acid as an activating agent. From a complete carbon balance perspective, the usage of phosphoric acid in the pre-treatment process presents an avenue to enhance the carbon retention value of the biochar material during the pyrolysis process. In turn, the reactions invoking carbon as well as phosphorus along with formation of crosslinking bonds (P-O-P), serve to fortify the overall stability of the carbon framework of the biochar material [27]. Consequently, biochar material subjected to phosphoric acid treatment bears the potential to sustain a greater amount of carbon within the framework, thereby augmenting the carbon sequestration capability.

4.3.2. Characterization of biochar obtained from kraft lignin

4.3.2.1. FTIR spectral study

It is perceived as an important tool to study the chemical compositions as well as functional groups present in the materials. On the grounds of various chemical compositions, the FTIR spectra of biochar as well as kraft lignin vary a bit. Kraft lignin, being an organic polymer derived from wood pulp, exhibited various characteristic peaks associated with different functional groups which are inclusive of -OH stretching vibrations at 3396 cm^{-1}, -CH stretching vibrations at 2919 cm^{-1}, -C=O stretching vibrations at around 1715 cm^{-1} and -C-O stretching vibrations at around 1114 cm^{-1}. The existence of these disparate functional groups indicated the organic nature of kraft lignin material. On the other hand, biochar being a carbonaceous material, exhibited a broad as well as a strong IR absorption peak at 3336 cm^{-1} and 2910 cm^{-1} which attributed to -OH as well as -CH stretching vibrations, respectively. In turn, the presence of very weak peaks in the 1700-1650 cm^{-1} range attributed to reduce the presence of carbonyl functional groups in the biochar material in comparison to Kraft lignin. Under the same context, the absence of strong FTIR peaks in the 1225-1015 cm^{-1} range corresponded to fewer -C-O functional groups in the biochar material. Moreover, the existence of a significant, broad FTIR absorption peak at 1630 cm^{-1} corresponded to the characteristic aromatic -C-C stretching vibrations, thereby reaffirming the formation of carbon-rich material, viz., biochar as illustrated clearly in **Figure 4.1. (a)** [28]. Therefore, the core difference in the FTIR spectra of biochar as well

as kraft lignin is the greater content of organic functional groups in lignin material, wherein biochar material is primarily composed of carbon with existence of few organic functional groups.

4.3.2.2. Raman spectroscopy

It is regarded as a powerful tool to conduct the characterization of chemicals as well as structural properties of different materials. The Raman spectroscopy of biochar typically highlighted two main peaks in the spectrum, viz., the D band and the G band. The G band situated at 1590 cm^{-1} corresponded to the graphitic carbon content of the biochar material whereas the D band at 1349 cm^{-1} referred to the presence of disorders or defects in the structure of biochar material. The I_D/I_G ratio provided a clear depiction on the degree of graphitization as well as structural disorder. In this context, it was found to be 0.84 which indicates a high degree of graphitization along with a more orderly graphite structure of the biochar material as displayed in **Figure 4.1. (b)** [29].

4.3.2.3. PXRD analysis

This technique provides an assessment of the structural attributes of biochar material. In turn, it also helps in understanding the existence of different crystalline materials that play a crucial role to influencing the features of biochar material. The XRD patterns of biochar as shown in **Figure 4.1. (c)** typically illustrated the broad diffraction peaks on ground of amorphous nature of biochar material, occurring from charring as well as incomplete combustion of organic materials during pyrolysis procedure. The peak at $2\theta = 23.34°$ referred to the disordered graphitic carbon structure, whereas other peaks at $2\theta = 30.88°$, 31.53°, 32.18°, 34.63°, 35.46° and 37.42° depicted the existence of crystalline phase of calcite. Moreover, other peaks at $2\theta = 21.69°$ and 17.43° indicated the lines of diffraction of quartz material (SiO_2) and unreacted lignin particles, respectively [29].

4.3.2.4. BET analysis

The BET (Brunauer-Emmett-Teller) method is used to assess the specific surface area of various porous materials, including biochar. This technique provides useful information about various surface properties of biochar, which can be useful for conducting different applications. The specific surface area is found out to be 1038.35 m^2/g along with a pore volume of 0.118 cm^3/g and pore size of 3.85 nm as obtained from the BJH

(Barrett-Joyner-Halenda) desorption results [30]. A higher specific surface area value depicts potentially more reactive as well as more porous biochar materials. In turn, the pore size distribution studies revealed that the synthesized biochar material possessed pores which are mesoporous in nature as their pore size falls within the ambit of 2-50 nm. Furthermore, the N_2 adsorption-desorption isotherm as shown in **Figure 4.1. (d)** also indicated greater N_2 adsorption at lower partial pressure which further enumerated filling up of the mesopores, and the existence of a hysteresis between 0.54 and 0.75 relative pressure further substantiated the fact that the biochar material possessed mesopores as reported in various studies [26].

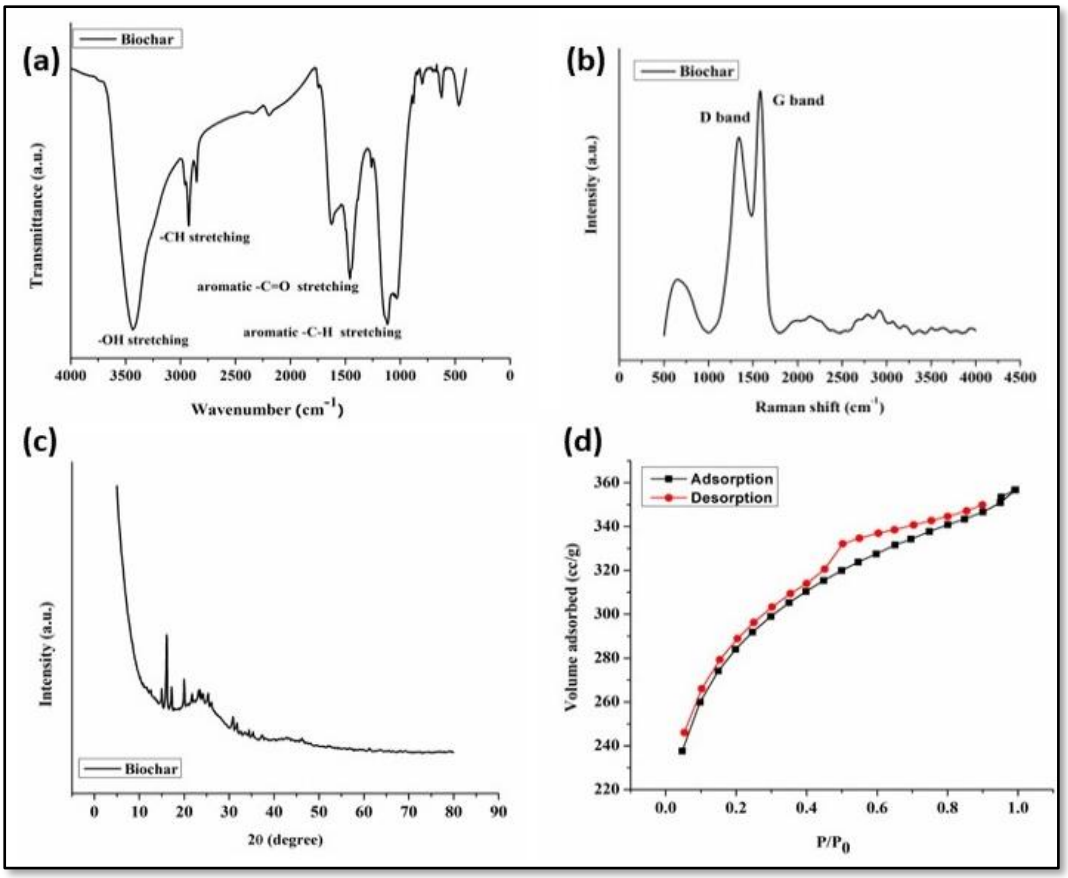

Figure 4.1. (a) FTIR spectra, **(b)** Raman spectra, **(c)** PXRD spectra, and **(d)** BET adsorption-desorption curves of biochar material.

4.3.2.5. XPS analysis

This technique provides useful information about the elemental surface composition, functional groups and chemical bonding of the biochar material. A meticulous study of the XPS spectra demonstrated the existence of O and C as the core elements along with P, S

and Al in trace amounts. The atomic fractions of these elements were found out to be 78.48%, 20.02%, 1.02%, 0.35% and 0.13%, respectively. In turn, comprehensive assessment was conducted by invoking the high-resolution spectra of C 1s, O 1s, P 2p and S 2p. Under this context, the C 1s spectrum was deconvoluted into three major peaks centered at 284.1 eV, which is assigned to C-C (sp^2); at 286.3 eV, which is conferred to C-O; and at 287.2 eV, which is attributed to C=O, respectively. The existence of these peaks substantiated the presence of carbon double bonded with oxygen in carbonyl and quinone like structural entities. Furthermore, the O1s spectrum was deconvoluted into two major peaks which were further designated categorically to C-O at 531.8 eV and C=O at 532.9 eV, respectively [15]. Similarly, the S 2p spectrum was deconvoluted into two core peaks which are assigned particularly to oxides of sulfur at 169.2 eV and sulfur (0) peak at 164.5 eV, respectively. Phosphorus and aluminum also displayed their corresponding XPS peaks at 134.21 eV and 72.8 eV, respectively [25].

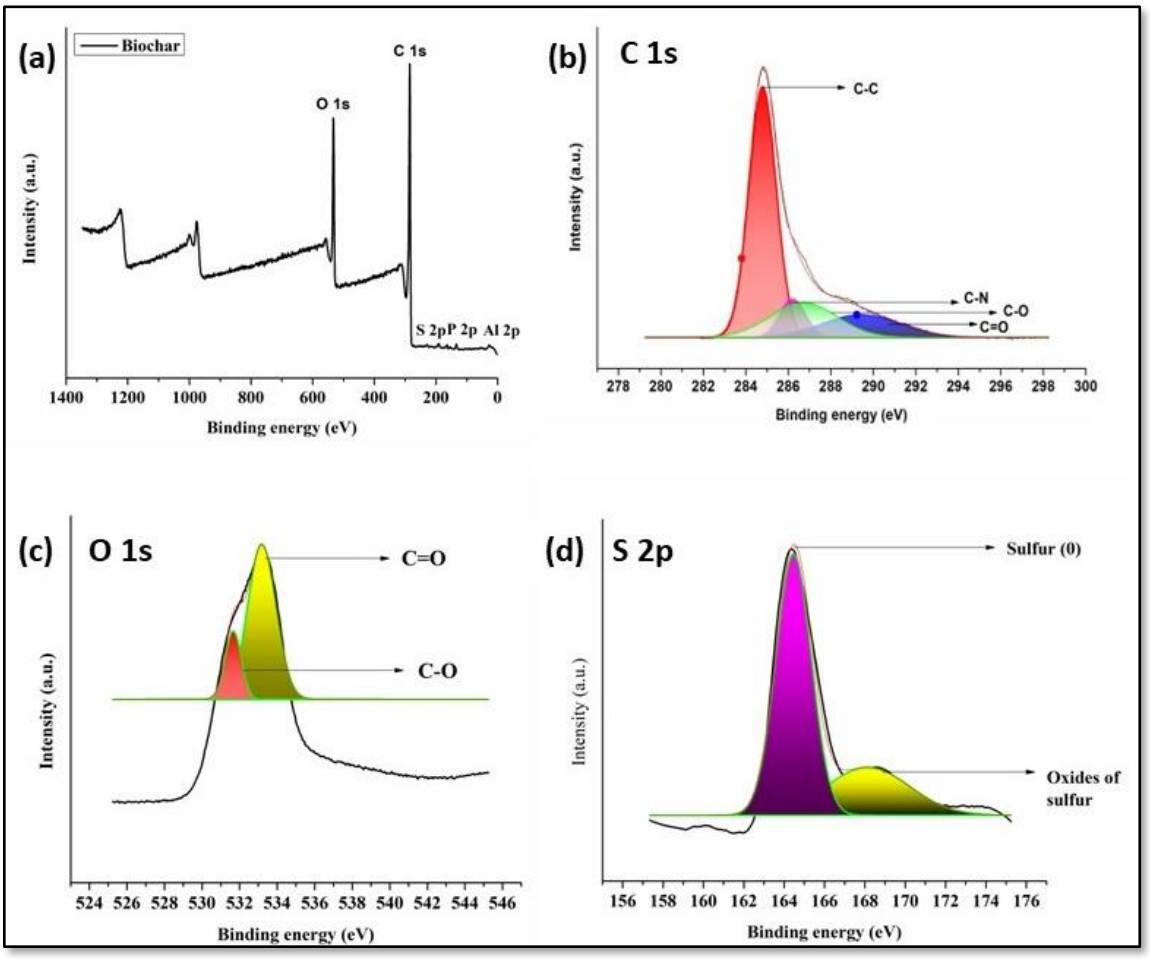

Figure 4.2. (a) XPS survey spectra, **(b)** C 1s, **(c)** O 1s, and **(d)** S 2p high-resolution spectra for biochar material.

4.3.2.6. Proximate and ultimate analysis

The proximate analysis of biochar was conducted to evaluate the core chemical composition of the material. It involved determining various parameters, viz., fixed carbon proportion, moisture content, volatile matter, ash amount, etc. **Table 4.2**. provided comprehensive detailed information on all the aforementioned variables. As previous reports suggest, increment in pyrolysis temperature results in lowering the volatile matter content on ground of complete carbonization process. In turn, an increase in carbonization temperature culminates in overall increment of the ash content with subsequent decrease in the fixed carbon amount. Other studies further reveal that enhancement in pyrolysis temperature within the ambit of 400 to 800 °C, yields notable decrement in the content of volatile matter which can be attributed to the aromatization method, enrichment of different inorganic minerals as well as degradation of different lignocellulosic components. These findings perfectly align with the results reported by Domingues et al. and Wang et al. [24, 25] In our work, the biochar prepared from kraft lignin exhibited a high fixed carbon content, i.e., 85.58 wt% along with low ash and volatile matter amount and the results were found to be comparable with the reports of Nair et al. as well as Lee et al. [31, 32].

Table 4.2. Proximate analysis of biochar obtained from kraft lignin.

Moisture content (wt%)	**Volatile matter (wt%)**	**Ash (wt%)**	**Fixed C (wt%)**
6.24±0.12	5.12±0.02	3.06±0.01	85.58±0.35

The ultimate analysis of biochar invokes assessing the elemental composition, inclusive of different percentages of carbon, oxygen, sulfur, etc. The obtained results provide insights into the chemical composition of the biochar material. **Table 4.3.** demonstrated the outcomes of ultimate analysis carried out on biochar material prepared from kraft lignin. It was noted that the biochar possessed a higher mass fraction of carbon content of 74.29% along with 21.74% of oxygen content. The reason behind the increment in the carbon mass fraction can be attributed to the development of a condensed carbon entity resulting from polymerization reactions as well as the reduction of hydroxyl functional

groups present on the periphery of biochar material during the dehydration procedure. In turn, the H/C ratio was found out to be very low, i.e., 0.053 which is demonstrative of the fact that the synthesized biochar had a high degree of aromatization and carbonization. Additionally, the O/C ratio was observed to be notably low on ground of the elimination of the oxygen bearing functional moieties from the biomass matrix during the pyrolysis as well as the dehydration processes [32].

Table 4.3. Ultimate analysis of biochar obtained from kraft lignin.

C (wt%)	O (wt%)	H (wt%)	H/C	O/C
74.29	21.74	3.97	0.053	0.292

4.3.2.7. FESEM and EDX analysis

FESEM study was conducted to assess the morphology of the biochar material. According to the FESEM images as shown in **Figure 4.3. (a),** the biochar material demonstrated particle like nature at the nanometer scale which are consistent with literature studies reported earlier [23-25]. In addition, the biochar particles exhibited spherical morphology and the fineness of the particles on ground of its high surface area has led to the formation of some agglomerations, as evident from the FESEM images.

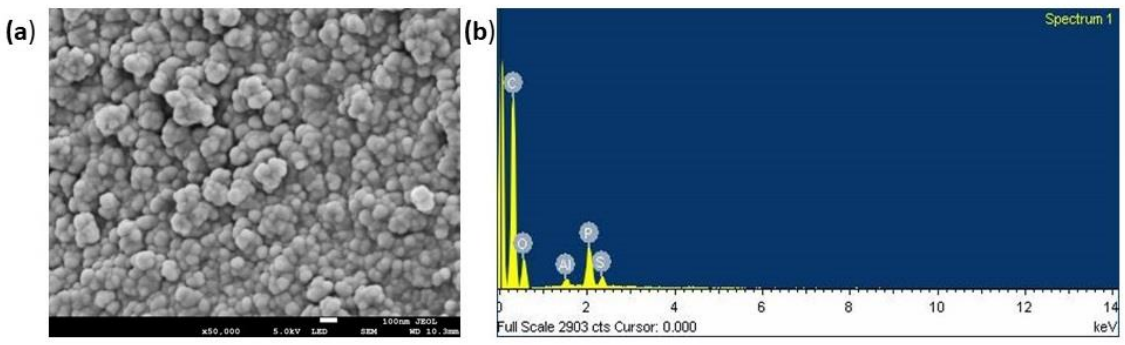

Figure 4.3. (a) FESEM images and, **(b)** EDX study of biochar material.

In turn, the EDX technique was employed to conduct elemental analysis on the biochar material. It allowed for identification as well as quantification of different elements present in the biochar. **Figure 4.3. (b)** illustrated the elemental distribution of the biochar and the weight percentages of the elements detected in the analysis were found out to be: C-

70.19%, O- 24.86%, Al- 0.48%, P- 3.55% and S- 0.92%. Moreover, the presence of carbon, oxygen, aluminum, phosphorus and sulfur were corroborated by XPS analysis as well as ultimate analysis, thereby supporting the EDX results. **Figure 4.4.** further depicted the elemental mapping of biochar which indicated well-dispersed carbon, oxygen, phosphorus, sulfur and aluminum on the surface of the sample, with carbon being the predominant element [27].

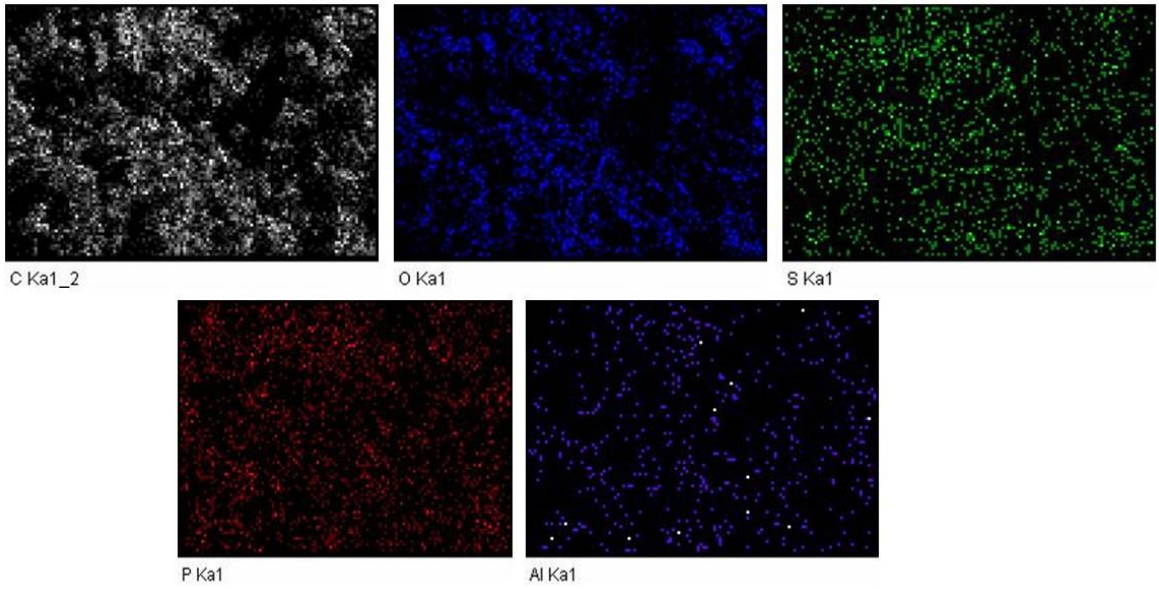

Figure 4.4. Elemental mapping of biochar material.

4.3.2.8. TEM analysis

This technique was employed to investigate the morphology of the biochar material derived from kraft lignin. The TEM analysis confirmed the spherical morphologies of the biochar particles as shown in **Figure 4.5.** In addition, the existence of these particles within the nanometer range is clearly confirmed by the TEM images. Consistent with the FESEM results, the TEM images also indicated huge agglomerations on ground of high surface area [21-23].

4.3.3. Fabrication of biochar/poly(ester amide urethane) nanocomposite

The biochar/poly(ester amide urethane) nanocomposites were fabricated invoking a one pot *in-situ* method, employing biochar as the reinforcing material. The primary synthesis of the base poly(ester amide) resin involved a polycondensation process between the prime

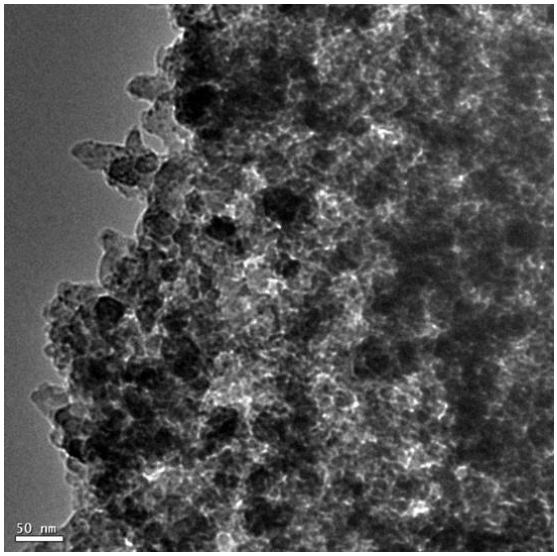

Figure 4.5. TEM analysis of biochar material.

substrates, viz., glycerol, citric acid, as well as hexamethylenediamine, detailed in **Chapter 2**. Employing a one-pot synthesis technique emphasized efficient time management, minimal chemical usage as well as simplified procedures for scalable industrial production. Since the resin exhibited somewhat brittle consistency, PVA and IPDI were introduced to strengthen the overall polymeric matrix via extensive hydrogen bonding interactions as well as polyaddition reactions between the isocyanate and hydroxyl functional groups. The introduction of urethane linkages into the base polymeric resin led to the formation of poly(ester amide urethane) resin as discussed extensively in **Chapter 3**. This was followed by the addition of biochar particles into the polymer matrix dispersed in minimal amount of DMSO solvent. The entire reaction, encompassing all the steps, occurred through uninterrupted mechanical stirring, ensuring the uniform blending of reactants and the biochar particles. Consequently, the polar moieties existing in the poly(ester amide urethane) resin interacted with the polar functional moieties of biochar particles, thus stabilizing the overall composite unit. This uniform distribution of the biochar particles within the poly(ester amide urethane) matrix contributed to the enhancement of various performance characteristics. Both hydrogen bonding as well as dipole-dipole interactions played crucial roles in facilitating interactions between biochar particles and polymer matrix. The oxygen from the hydroxyl or carbonyl group in biochar's functional moieties interacted with the hydrogen from the hydroxyl or urethane groups in the polymer matrix, forming extensive hydrogen bonds. This resulted in enhancement of adhesion trait between the polymeric matrix and the biochar particles,

thereby improving the overall compatibility of the composite unit. Additionally, the biochar possessed polar functional moieties which can further interact with the polar regions of the polymer matrix via dipole-dipole interactions. The negative and positive ends of the polar groups present in the polymer and the biochar aligned perfectly which resulted in generation of attractive forces of attraction between them. In turn, these interactions contributed to the overall intermolecular interactive forces between the polymer and biochar, thereby influencing the properties of the polymer nanocomposite.

4.3.4. Characterization of biochar/poly(ester amide urethane) nanocomposite

The nanocomposites produced underwent characterization invoking different spectroscopic as well as microscopic methods which are inclusive of FTIR, PXRD, XPS, and FESEM analyses.

4.3.4.1. FTIR spectral study

FTIR spectroscopy was assigned to identify the functional groups existing within the resinous polymer nanocomposites, and the findings were subsequently compared with the base polymer matrix. The analysis revealed that all the polymer nanocomposites demonstrated characteristic absorption peaks akin to those observed in poly(ester amide urethane) resin. This observation implied a similar chemical structure between the polymer nanocomposites and the polymer matrix [15]. Overall, the chemical compositions of the polymer nanocomposites deviated from the base polymer matrix solely on the ground of inclusion of biochar particles into the poly(ester amide urethane) resin.

Although, the FTIR spectra of the polymer nanocomposites and their various compositions were found to be similar, some notable changes were observed in the absorption bands corresponding to the hydroxyl groups. Specifically, the absorption bands for hydroxyl groups shifted to lower wavenumbers from 3456 to 3402 cm^{-1}, following the formation of the polymer nanocomposites which could be attributed to the increased number of polar-polar interactions, viz., hydrogen bonding, etc. between the polar functional moieties of biochar and poly(ester amide urethane) resin. Furthermore, peaks observed in the frequency range of 1600-1800 cm^{-1} and 1200-1300 cm^{-1} were identified as aromatic carbonyl stretching and C-O stretching of biochar material, respectively. In turn, the study observed that as the loading of the biochar material in the polymer nanocomposites

increased, the intensity of the C=O as well as C-O peaks became slightly more pronounced which confirmed successful incorporation of the reinforcing agent into the polymer nanocomposites. Lastly, IR absorption peaks in the frequency range of 2863-2941 cm^{-1} were identified as the symmetric as well as asymmetric sp^3 C-H stretching of the fabricated polymer nanocomposites [13-15]. The FTIR spectra as illustrated in **Figure 4.6. (a)** displayed all the aforementioned absorption peaks for all the compositions of biochar integrated poly(ester amide urethane) nanocomposites.

4.3.4.2. PXRD analysis

The PXRD analysis of the synthesized polymer nanocomposites was conducted in order to assess the various interactions occurring between the poly(ester amide urethane) resin and the biochar particles as shown in **Figure 4.6. (b)**. It was observed that all the studied nanocomposites exhibited XRD peaks within the ambit of 16.34-16.70° and 24.41-25.15°. Moreover, it was closely investigated that the peaks within the range of 24.41-25.15° were absent in the poly(ester amide urethane) resin devoid of any biochar particles. This confirmed successful incorporation of biochar material into the polymeric matrix as these

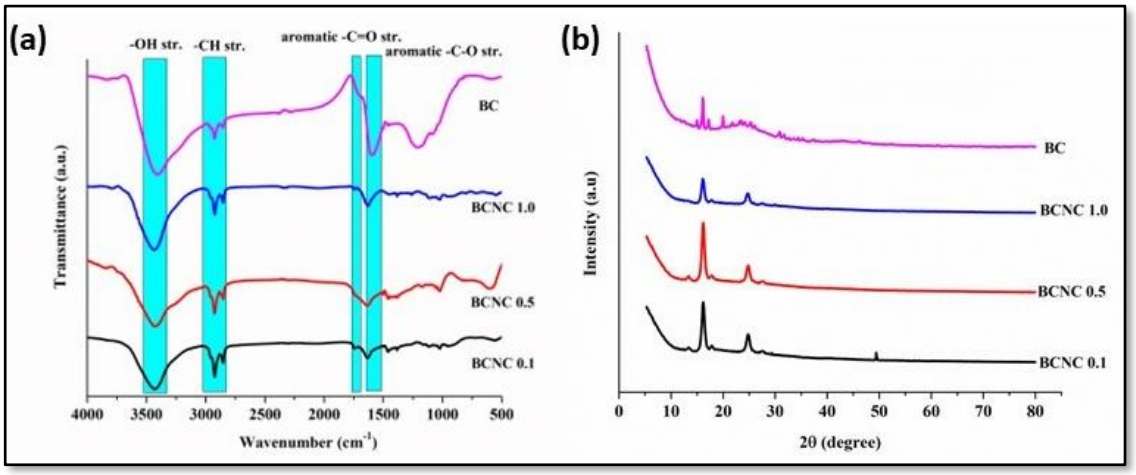

Figure 4.6. (a) FTIR spectra, and **(b)** PXRD spectra of biochar integrated poly(ester amide urethane) nanocomposites with different compositions.

XRD peaks referred to the disordered graphitic structure of carbon. In turn, the peaks observed within the range of 16.34-16.70° are attributed to the presence of PVA in the polymer matrix. Additionally, the shifts observed in the values of XRD peaks of PVA elucidated the denser crosslinked architecture of the polymer nanocomposites and is

indicative of the evolving structural features within the polymer nanocomposites as the content of the biochar material increased in the polymer matrix [33].

4.3.4.3. XPS analysis

This technique aids in furnishing valuable insights into the chemical bonding, elemental surface composition as well as functional groups of the polymer nanocomposites. A detailed examination of the XPS spectra revealed the predominant presence of O, C and N as the core elements, accompanied by trace amounts of S, P and Al as shown in **Figure 4.7. (a)**. The atomic fractions of these elements were determined to be 41.62%, 55.88%, 1.07%, 0.61%, 0.19% and 0.64%, respectively. The presence of these trace elements highlighted the successful incorporation of biochar particles into the polymer matrix. To further enhance the understanding, a comprehensive assessment was carried out by examining the high-resolution spectra of C 1s, O 1s, N 1s, S 2p and P 2p. In this context,

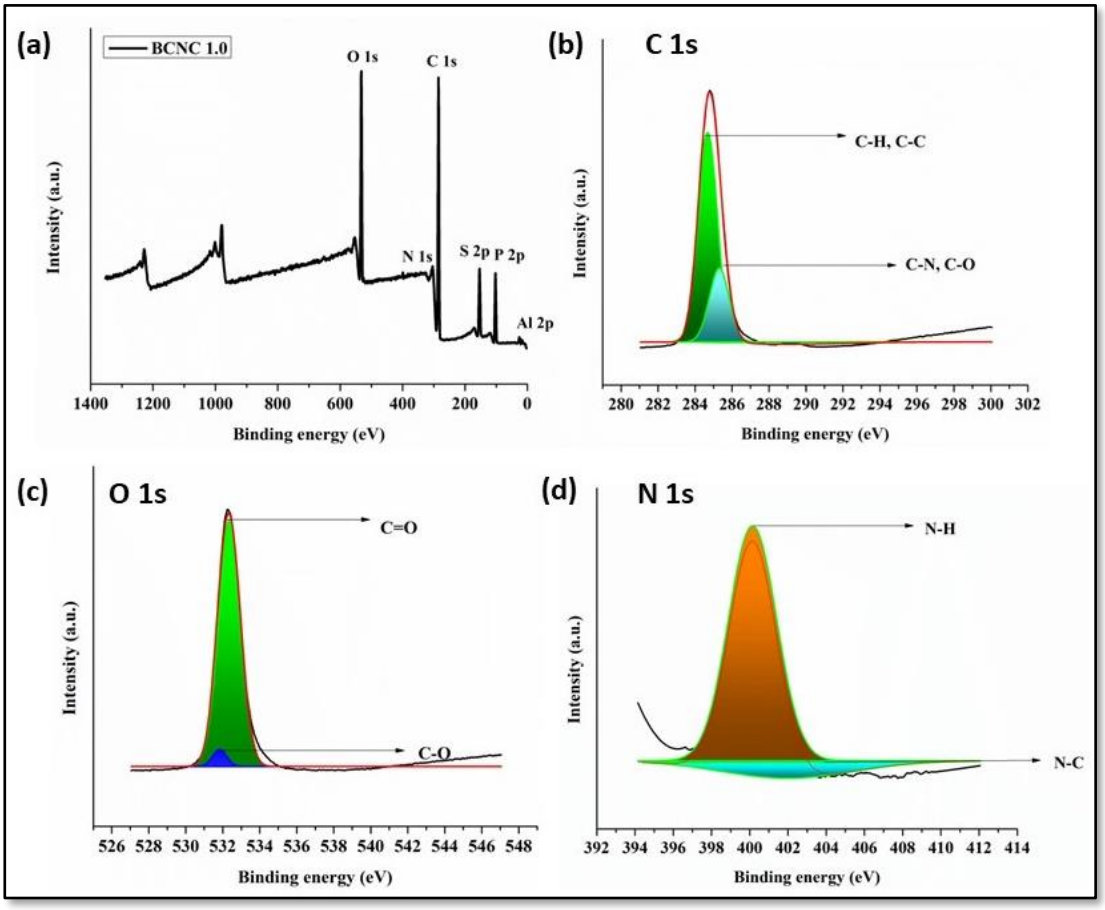

Figure 4.7. (a) XPS survey spectra, **(b)** C 1s, **(c)** O 1s, and **(d)** N 1s high-resolution spectra for biochar integrated with poly(ester amide urethane) nanocomposites.

the C 1s spectrum underwent deconvolution, which resulted in three prominent peaks situated at 284.78 eV (attributed to C-H, C-C groups), 285.30 eV (associated with C-N, C-O groups), and 287.10 eV (assigned to C=O groups) as depicted in **Figure 4.7. (b)**. All these spectral peaks were evaluated as representative peaks of carbon containing moieties, viz., glycerol, citric acid, hexamethylenediamine, biochar, etc. Additionally, the O 1s spectrum was deconvoluted into two major peaks categorically assigned to C=O at 532.22 eV and C-O at 531.65 eV. This deconvolution further elucidated the specific oxygen-containing functional groups present in the polymer nanocomposites as highlighted in **Figure 4.7. (c)**. Moreover, the N 1s spectrum underwent deconvolution into two peaks at 397.53 eV and 400.11 eV which were accredited to N-C and N-H moieties, respectively as illustrated in **Figure 4.7. (d)**. These peaks aid in establishing the existence of IPDI and hexamethylenediamine entities in the composites. Furthermore, sulfur, aluminum and phosphorus exhibited their corresponding XPS peaks at 168.42 eV, 73.21 eV and 135.23 eV, respectively. These peaks substantiate successful fabrication of the polymer nanocomposites integrated with the reinforcing agent, viz., the biochar particles [17].

4.3.4.4. FESEM analysis

The microscopic analysis of the synthesized polymer nanocomposites was conducted using FESEM technique. The FESEM images as depicted in **Figure 4.8.** revealed a comprehensive view of the biochar particles uniformly integrated as well as distributed within the poly(ester amide urethane) matrix. The polymeric surface exhibited a textured appearance due to the presence of the embedded biochar particles (spherical dots), thereby demonstrating an interconnected and well-dispersed network throughout the polymeric material [16]. Thus, the interplay between the polymer matrix and the biochar material is clearly evident; showcasing a cohesive integration which is essential for achieving enhanced properties of the material. Thus, these micrographs enumerated the successful incorporation of these biochar particles within the poly(ester amide urethane) matrix.

4.3.5. Mechanical properties

The superior performance of any polymeric material is certainly contingent upon their mechanical properties, as these features not only proclaim durability but also aid in ascertaining their viability for diverse applications. Different polymer nanocomposites enriched with various nano-sized reinforcing agents demonstrate enhanced mechanical

properties in comparison to their unmodified counterparts. In this milieu, biochar, alongside other eco-friendly materials have garnered significant attention from material

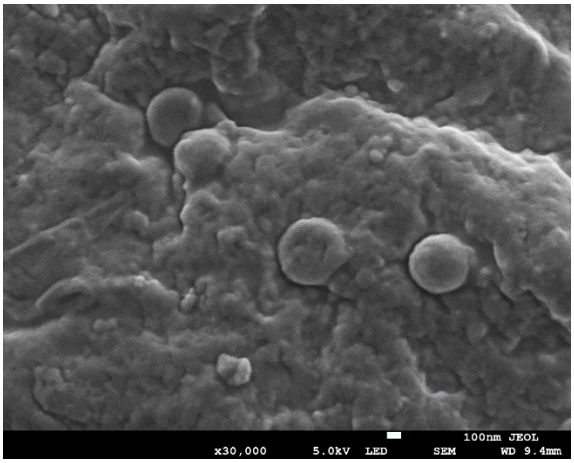

Figure 4.8. FESEM images of biochar integrated poly(ester amide urethane) nanocomposites.

scientists for its potential utility as a reinforcing agent in polymer matrices. Consequently, this rationale underscores the incorporation of biochar particles derived from kraft lignin into the poly(ester amide urethane) resin. The fabricated poly(ester amide urethane)/biochar nanocomposites exhibited significantly improved mechanical properties as compared to the poly(ester amide urethane) resin, as detailed in **Table 4.4.**, along with their stress-strain profiles presented in **Figure 4.9.** Notably, a noteworthy enhancement in mechanical properties is evident even at low loadings of biochar particles, ranging from 0.5 wt% to 1.0 wt% in the poly(ester amide urethane) resin. Subsequently, a loading dependent trend was observed, wherein the mechanical properties of the polymer nanocomposites consistently rose with an increased quantity of biochar particles in the polymer matrix [23-26]. The tensile strength and elongation at break values were observed to fall within the range of 4.31-6.25 MPa and 1754.2-2100.3%, respectively, following the incorporation of the biochar particles. This increment in mechanical variables contributed to an overall toughness enhancement, ranging from 80.17-90.22 MJ/m^3, obtained from the area under the respective stress-strain curves. Similarly, the impact resistance of the polymer nanocomposites was found to improve with an increment in the loading amounts of biochar particles. In turn, the scratch hardness parameter for all the compositions of the polymer nanocomposites also increased in its value compared to the core polymer resin; however, all of them exhibited similar values without any stark difference, thereby attaining the maximum limit of the instrument. Consequently, these results lead to the

ultimate conclusion that BCNC 1.0 exhibited superior mechanical toughness as compared to BCNC 0.1 and BCNC 0.5.

Table 4.4. Mechanical properties of the fabricated poly(ester amide urethane) nanocomposites.

Sample	BCNC 0.1	BCNC 0.5	BCNC 1.0
Tensile strength (MPa)	4.31 ± 0.61	4.75 ± 0.85	6.25 ± 0.77
Elongation at break (%)	2100.3 ± 1.92	1987.5 ± 2.10	1754.2 ± 0.58
Toughness (MJ/m^3)	80.17 ± 20.3	84.43 ± 34.8	90.22 ± 9.0
Impact strength (kJ/m)	16.9 ± 1.2	20.1 ± 1.4	22.7 ± 2.7
Scratch hardness (kg)	8.0 ± 0.5	8.0 ± 0.5	8.5 ± 0.5

The increased tensile strength values observed in the polymer nanocomposites can be attributed to the fine surface area of biochar particles as well as their distinctive chemical structure, along with their uniform dispersion within the poly(ester amide urethane) matrix. The substantial surface area of biochar material coupled with the presence of various functional groups on its surface established its efficacy as a potent reinforcing agent. Furthermore, these polar functional moieties within the polymer nanocomposite engage in diverse interactions, viz., hydrogen bonding, dipole-dipole interactions, etc. with the hydroxyl, urethane and carboxyl entities present in the poly(ester amide urethane) matrix during the in-situ fabrication method. These interactions help in enhancing the physico-mechanical interlocking mechanism through chain entanglement within the polymer matrix, resulting in enhancement of rigidity along with reduction in free volume. Consequently, when any particular force gets applied to the polymer nanocomposites, it gets uniformly distributed across the entire poly(ester amide urethane) matrix and its composite, thereby demonstrating high tensile strength values on ground of synergistic effect. For instance, Idrees et al. in 2018 carried out a study using PET incorporated with

5 wt% biochar particles. The composite material exhibited superior tensile strength in comparison to pure PET material on the ground of effective interfacial bonding between the additive and the polymer matrix [34]. Nevertheless, it was also noted that lower loadings, viz., 1 wt% resulted in higher tensile strength values on account of efficient homogeneous dispersions and reduced agglomeration levels. Similarly, Li et al. in 2018 used biochar as an additive (60 wt%) in conducting fabrication of a high molecular weight as well as low density polyethylene composite with manifold increment in tensile strength values [35]. On a similar ground, Nan et al. observed a reduction in the ductility of PVA with the introduction of biochar material [36]. Despite this decrease in the flexibility values, there was a concurrent elevation in the tensile modulus parameter which is indicative of the polymer's toughness parameter. This enhancement was attributed to the inherent rigidity provided by biochar itself, surpassing that of PVA material.

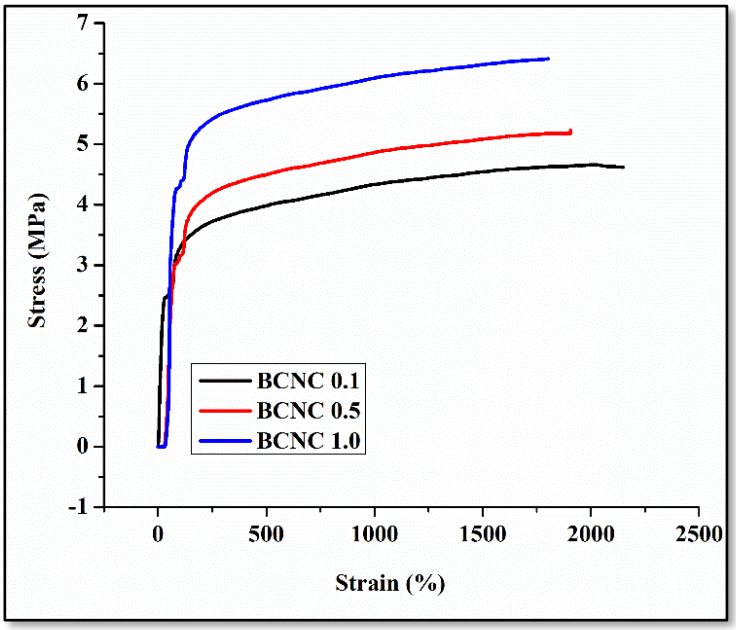

Figure 4.9. Stress-strain profiles for all compositions of biochar integrated poly(ester amide urethane) nanocomposites.

4.3.6. Thermal properties

The assessment of thermal durability holds considerable significance in conducting the evaluation of the degradation characteristics as well as the thermal stability of different polymer nanocomposites for manifold applications in diverse genres. In this context, the thermal stability and the degradation behavior of all formulated polymer nanocomposites were ascertained through TG analysis. In turn, the corresponding TG thermograms,

complemented by their derivative curves, viz., dTG for all the compositions of polymer nanocomposites are depicted in **Figure 4.10. (a)** and **(b)**, respectively. Additionally, all the pertinent information, viz., char residues, onset temperature and peak degradation temperatures at 600 °C has been systematically compiled in **Table 4.5.** The examination revealed that the polymer nanocomposites exhibited stability within the temperature range of 203-205 °C; thereby surpassing the stability of the poly(ester amide urethane) resin devoid of any biochar particles, which remained stable only up to 170.41 °C, denoted as T_{ON} temperature [15]. In turn, all the TG thermograms of all compositions of the nanocomposites along with the pristine polymeric resin manifested a two-step degradation pattern akin to that observed in the bare poly(ester amide urethane) resin. This is suggestive of the fact that the incorporation of biochar particles into the poly(ester amide urethane) resin did not exert any such discernible influence on the overall structural characteristics of the polymer composites. Nevertheless, there existed some prime variations in the peak degradation temperatures within each degradation step of the polymer nanocomposites.

Table 4.5. Thermal degradation variables for polymer nanocomposites with various compositions.

Variables	PEAU	BCNC 0.1	BCNC 0.5	BCNC 1.0
T_{on} (°C)	170.41	203	203.54	205
1st stage degradation peak temperature (°C)	186.39	262.73	263.01	265
2nd stage degradation peak temperature (°C)	472	419	422	435
Weight residue (%) at 600 °C	19.07	29.02	30.02	31.72
Glass transition temperature, T_g (°C)	-28.15	79	82	84

The peak temperature associated with the first step degradation, attributed to the presence of different labile linkages, viz., aliphatic segments, ester moieties, etc., demonstrated a gradual increment from 186.39 °C for poly(ester amide urethane) resin to 313 °C for BCNC 1.0. This rise in degradation temperature, following the incorporation of the biochar

particles into the polymer matrix, was linked to the presence of different polar functional groups on the periphery of the biochar material. These groups contributed to the formation of a greater number of labile linkages during the fabrication procedure. In fact, biochar, inherently endowed with exceptional thermal stability, stands as a testament to its robustness, a fact substantiated by various reports. For instance- Nan et al. in 2016 observed a noteworthy delay in the weight loss as well as thermal degradation temperature of PVA upon incorporation of biochar into the polymer matrix. This delay was attributed significantly to the superior thermal stability existing inherently in the biochar particles [36, 37]. On a similar context, the peak temperatures of the second step degradation, associated with the presence of amide, urethane and aromatic moieties in the polymer matrix, experienced a significant increment from 419 °C for BCNC 0.1 to 435 °C for BCNC 1.0 on ground of incorporation of the biochar particles. Furthermore, an increase in the loading amounts of the polymer nanocomposites resulted in higher peak temperatures for both the first and second degradation steps. This observation can be explained on the ground of increment in the number of polar functional groups. Consequently, it can be affirmed from these observations that the polymer nanocomposites exhibited enhanced thermal stability compared to the bare material, and their thermostability augmented with the increasing amount of incorporation of biochar into the polymer matrix. This conclusion finds support in the percentage of weight residues of the polymer nanocomposites at 600 °C, which measured for poly(ester amide urethane) resin and 29.02%, 30.02% and 31.72% for BCNC 0.1, BCNC 0.5 and BCNC 1.0, respectively.

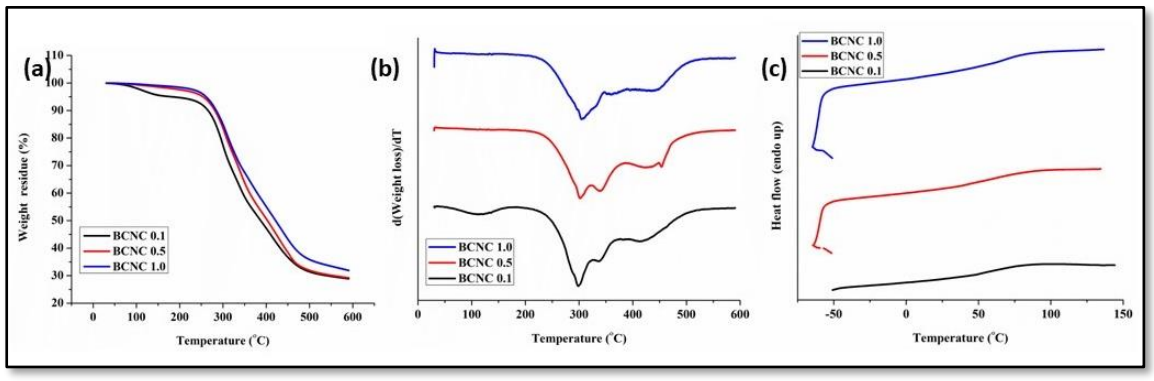

Figure 4.10. (a) TGA, **(b)** dTG, and **(c)** DSC profiles of the nanocomposites with their various compositions.

DSC studies were undertaken to determine the T_g value of the polymer nanocomposites, as demonstrated in **Figure 4.10. (c)**, which revealed a temperature range of 79-84 °C. Notably, the introduction of the biochar particles into the polymer matrix resulted in causing increment of T_g values from 79 °C for BCNC 0.1 to 84 °C for BCNC 1.0 compared to the pristine poly(ester amide urethane) resin (T_g: -28.15 °C). This can be attributed to the rampant increase in cross-linking values on ground of enhanced intermolecular forces of attraction between the biochar particles and the polymer matrix. Subsequently, it resulted in a decrease in the free volume along with restricted mobility, causing an increase in T_g values [15, 16].

4.3.7. Biodegradation study

An accelerated biodegradation investigation was conducted on the polymer nanocomposites in order to evaluate their potency as a biodegradable material. The study invoked targeting one bacterial strain, viz., *Bacillus subtilis*, and this was followed by monitoring the optical values in the presence of these composites over time. Notably, all the compositions of the polymer nanocomposites exhibited higher absorbance values as enumerated in **Figure 4.11. (a)**. Furthermore, a discernible trend was noted down wherein the optical values gradually escalated with an augmentation in the biochar loadings, thereby indicating increased biodegradability levels linked to an increase in the abundance of biochar particles. The inclusion of biochar particles, endowed with various polar functional groups, facilitated interactions with different polar moieties of the polymer matrix, resulting in the formation of labile linkages, viz., hydrogen bonding as well as ester linkages. Consequently, these supplementary linkages in the nanocomposites underwent hydrolysis by the bacterial strain, inducing extensive surface erosion and thereby enhancing the rate of biodegradation compared to the bare polymer resin. The weight loss profiles as depicted in **Figure 4.11. (b)** illustrated the fact that the augmentation in biochar loadings corresponded to an increment in the number of hydrolysable linkages within the polymer nanocomposites, leading to a proportional acceleration in the degradation rate as well as extensive weight loss. The SEM images as shown in **Figure 4.11. (c) and (d)** further highlighted the extent of bacterial growth (*Bacillus subtilis*) on the various compositions of polymer nanocomposites and were subsequently compared with the control sample (devoid of any bacterial strain).

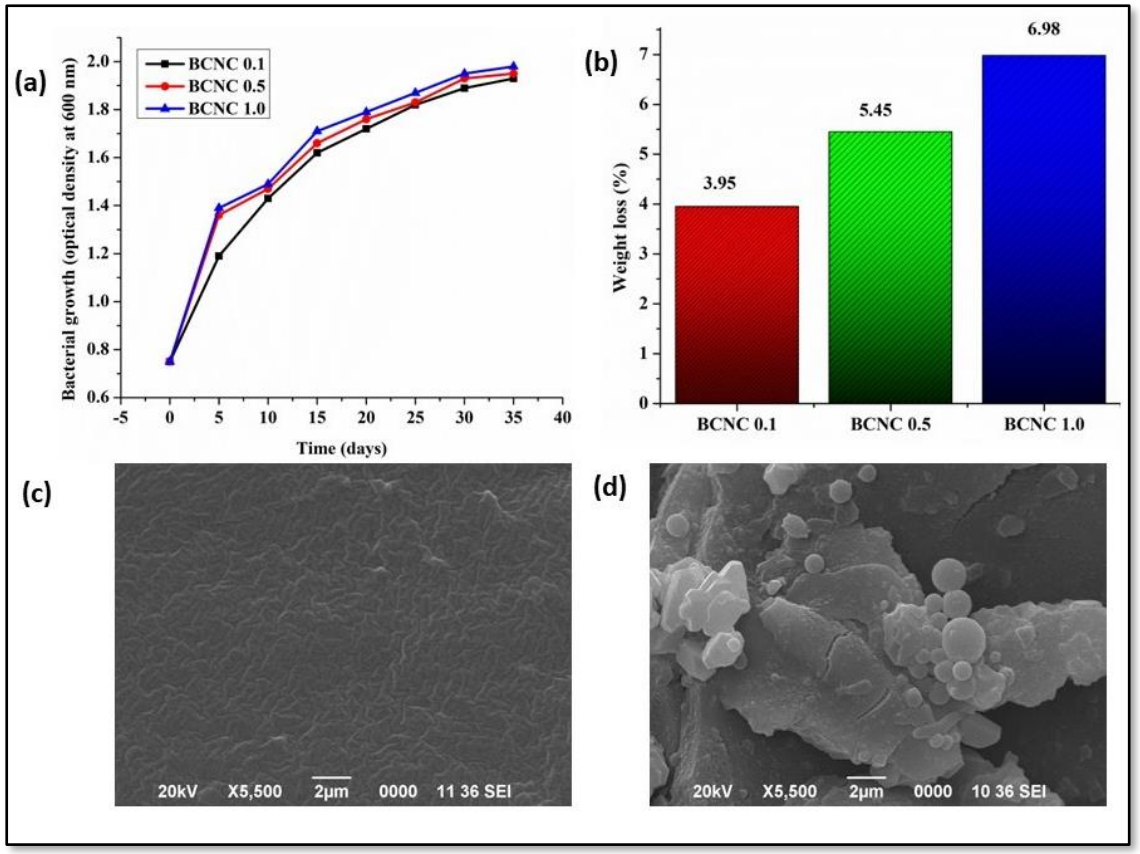

Figure 4.11. (a) Bacterial growth curves presented in terms of optical density as a function of time, **(b)** weight loss (%) of polymer nanocomposites after exposure to bacterial degradation, SEM images of BCNC 1.0, **(c)** control specimen, and **(d)** biodegraded by bacterial strain, *Bacillus subtilis.*

4.3.8. Dye adsorption

In order to assess the efficacy of the fabricated polymer nanocomposites as adsorbents, dye adsorption evaluation was conducted. The biochar material obtained from kraft lignin that exhibited the capability to interact with both the cationic as well as anionic groups of dye entities via electrostatic forces of interaction. Specifically, the anionic dye, tartrazine (TZ) and the cationic dye, malachite green (MG) were selected for undergoing this investigation. Among all the compositions of poly(ester amide urethane) nanocomposites, BCNC 1.0 was employed as the representative polymer nanocomposite for all the adsorption assessments. It is well-acknowledged that the removal efficiency is contingent upon various factors for all soluble dyes which are inclusive of pH, initial concentration of dye molecules, adsorption time, etc. A comprehensive exploration of the impact of these

factors on adsorption of dyes was conducted to derive the optimal adsorption outcomes.

4.3.8.1. Effect of adsorbent dose

The impact of adsorbent dosages on the removal efficiency (%) as well as on the adsorption amount of MG and TZ is depicted clearly in **Figure**. **4.12. (a)** and **(b)**. As observed, the adsorption (%) or removal efficiency increased proportionally with elevated adsorbent dose, thereby reaching a peak of 99.26% and 87.25%, with a 40 mg dosage for MG and 88.73% and 73.98%, with a 40 mg adsorbent dosage for TZ, for biochar and polymer nanocomposites, respectively. This enhancement in adsorption (%) is ascribed to the amplified presence of polar functional groups on the biochar material, thereby augmenting the availability of active adsorbent sites with an increment in the adsorbent dosages. **Figure. 4.12. (a)** and **(b)** also illustrated the influence of adsorbent dosages on the adsorbent amount or adsorption capacity(q_e). It was noted that despite an increase in the adsorption (%) from 95.32% to 99.26% and 72.27% to 87.25% for MG, as well as 74.76% to 88.73% and 58.45% to 73.98% for TZ, (for both biochar and polymer nanocomposites), the q_e parameter showed a declining trend. Consequently, considering both the parameters, viz., q_e variable as well as removal efficiency, the optimized dosages for both MG and TZ dyes were ascertained to be 40 mg, respectively. Furthermore, with these optimized adsorbent dosages, the adsorption capacity of the poly(ester amide urethane) nanocomposites for all the three compositions, for both the dyes were assessed as

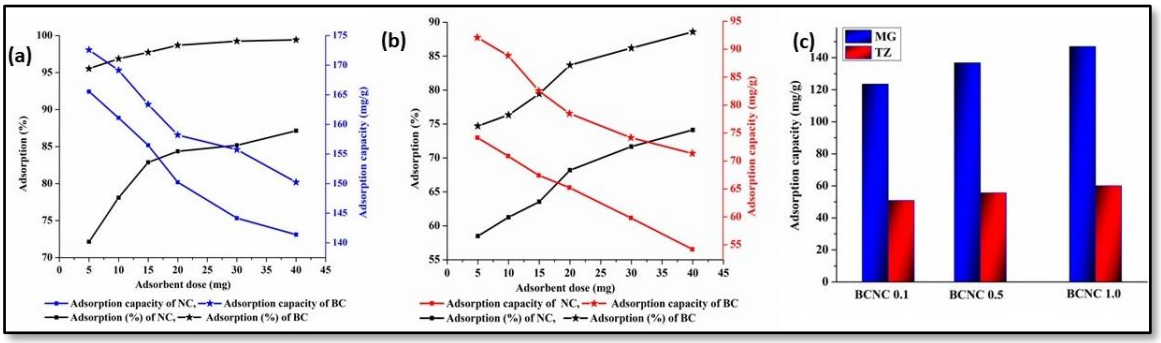

Figure 4.12. Effect of adsorbent dose on adsorption capacity (mg/g) and adsorption (%) of **(a)** MG dye, **(b)** TZ dye, and **(c)** adsorption capacity of various compositions of polymer nanocomposites for both MG and TZ dyes.

enumerated in **Figure 4.12. (c)**. As anticipated, the dye adsorption capacity for MG increased with an elevated proportion of biochar particles into the polymer matrix, owing to the augmented negative charge in the polymer matrix. Consequently, BCNC 1.0 exhibited the highest adsorption capability for MG, i.e., 142.12 mg/g, wherein adsorption declined gradually for BCNC 0.1 as well as BCNC 0.5. Likewise, BCNC 1.0 demonstrated the highest adsorption capacity for TZ, i.e., 56.51 mg/g; however, the values are lower on the ground of TZ being an anionic dye. These results strongly corroborated with the findings reported earlier [37, 38].

4.3.8.2. Effect of preliminary dye concentration

The impact of varying initial concentrations of dye, ranging from 10 ppm to 80 ppm, on the polymer nanocomposite's adsorption performance was thoroughly examined while maintaining the optimized adsorbent amount. As illustrated in **Figure 4.13. (a)** and **(b)**, it is quite evident that an escalation in dye concentration led to an increment in the adsorption amount. However, a corresponding reduction in adsorption efficiency was noted down, decreasing from 88.62% to 85.04% for MG and from 73.58% to 72.30% for TZ as illustrated in **Figure 4.13. (a)** and **(b).** This phenomenon can be rationalized by acknowledging the fact that at lower concentration of dye of 10 ppm, an abundance of active adsorption sites contributed to the overall greater percentage of adsorption [39]. Conversely, as the dye concentration increased, the availability of active adsorption sites on the surface of the polymer nanocomposites diminished. Consequently, a lower percentage of adsorption was noted at higher concentrations of dye.

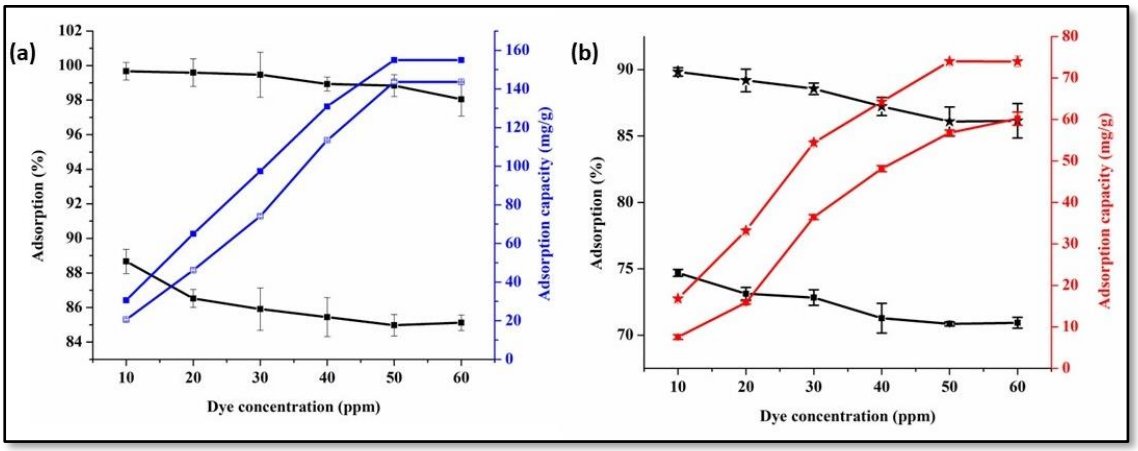

Figure 4.13. Effect of dye concentration on adsorption capacity (mg/g) and adsorption (%) for **(a)** MG dye, and **(b)** TZ dye

4.3.8.3. Effect of contact time

Figure 4.14. (a) and **(b)** illustrated the temporal influence on the removal efficiency of dye for polymer nanocomposites. The equilibrium time for adsorption was ascertained to be minutes for both MG and TZ. Beyond these specific durations, dye adsorption reached a plateau, indicating the attainment of equilibrium. Notably, the rate of adsorption is more pronounced in the preliminary stages compared to the period leading up to the equilibrium. This observation suggested that at an initial point of time, there might be electrostatic forces of interactions between the charged active sites of the polymer nanocomposites as well as the biochar particles. Following these interactions, mass transfer of dye molecules was observed involving both hydrogen bonding as well as other dipole-dipole interactions. All these results conformed with other studies reported earlier [38, 39].

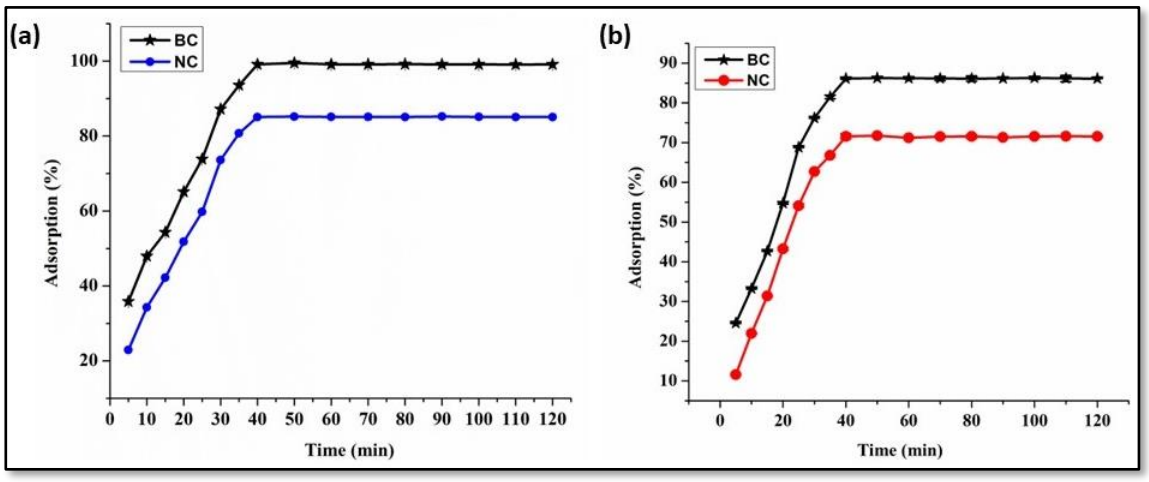

Figure 4.14. Effect of contact time on adsorption (%) for **(a)** MG dye, and **(b)** TZ dye.

4.3.8.4. Effect of pH

In order to investigate the pH sensitivity of poly(ester amide urethane) nanocomposites, the study was carried out under various pH conditions varying from 2 to 12 in the dye mixture. **Figure 4.15. (a)** illustrated the dye removal capacity of the polymer nanocomposites at various pH levels for MG dye. The graph enumerated that the optimal removal capacity of dyes occurred within the pH range of 4 to 8. Specifically, at pH 2, the adsorption (%) was found out to be 68.41%, which gradually escalated to 84.72% at pH 6. However, under basic pH conditions, viz., pH 10 and 12, the dye removal efficiency dropped down significantly to 59% and 51.09%, respectively. This phenomenon can be explained by the fact that under acidic conditions (lower pH), the biochar develops a

positive charge on its periphery on ground of the presence of some H_3O^+ ions, which significantly cause a drop in the removal efficiency of dye moieties. Since MG is a cationic dye, there exists a strong repulsive force between the dye molecules and the adsorbent surface. In turn, a strong competition arises between the H_3O^+ ions and the dye molecules. Furthermore, with the increment in the pH values, the hydroxyl as well as carboxyl functional groups present on the adsorbent surface create a negative atmosphere, thereby facilitating attraction of cationic dye entities. In turn, it was noted that at higher alkaline pH conditions, the removal efficiency of dyes was found to be low, which aligned with similar studies reported by other researchers. The increment in pH conditions resulted in reduction of the ionization potential of the functional groups, subsequently causing reduction in the removal efficiency of dyes [40].

On the contrary, for TZ dye, the trend for dye removal efficiency vs pH was observed to be opposite. As depicted in **Figure 4.15. (b)**, it was evident that with the increment in pH values, there was reduction in the adsorption (%) of TZ dyes from 71.09% at pH 2 to 39.62% at pH 12. The reason behind this can be explained on the ground that, at low pH values, the amine groups of the polymer nanocomposites get protonated to NH_2^+, which facilitate the attraction of TZ dye molecules, which are anionic in nature [41]. Additionally, the increment in pH values results in deprotonation of these amino groups, resulting in generation of intense repulsive forces, thereby causing reduction in the dye removal efficiency.

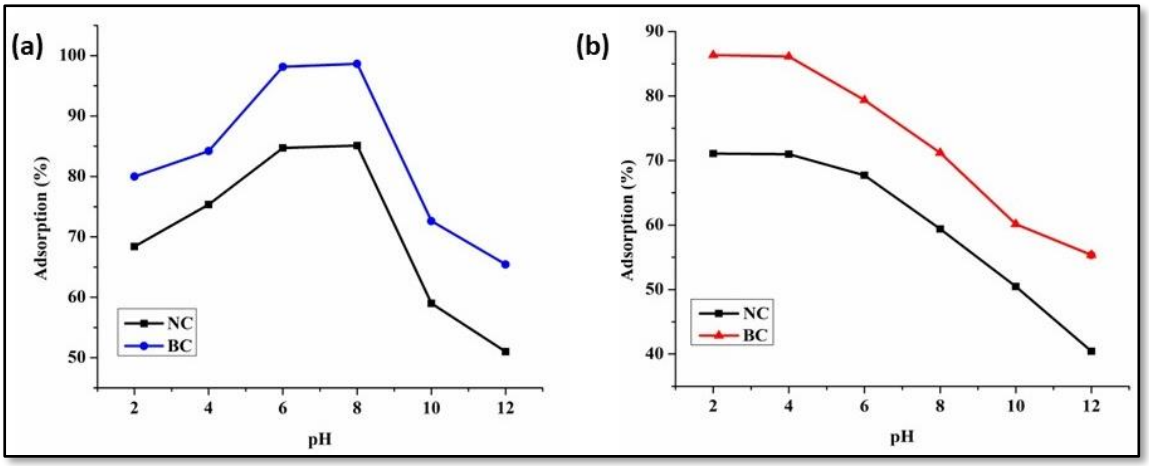

Figure 4.15. Effect of pH on adsorption (%) for **(a)** MG dye, and **(b)** TZ dye.

4.3.9. Kinetics study

Adsorption kinetics as a crucial parameter for ensuring anticipation of the adsorption phenomenon and gauging the rate at which adsorption occurs. In addition, the contact time required to achieve equilibrium holds immense importance in the context of adsorption dyes in practical applications in diverse realms. It was observed that throughout the adsorption process, molecules of the adsorbate migrate from the solution to the outer surface of the adsorbent molecules, followed by diffusion into the outline of the boundary, and ultimately, complete mass transfer occurs by internal pore diffusion process [38]. Furthermore, in order to elucidate the adsorption mechanism, exploration of the PFO model, PSO model and IPD model were carried out extensively. The linear versions of these models are clearly highlighted by equations **4.3, 4.4** and **4.5**, respectively. Under this context, **Figure 4.16.**, depicted the linear plots illustrating $\log(q_e-q_t)$ against t, (t/q_t) against t for PFO and PSO models, respectively and q_t against $t_{1/2}$ for IPD model are presented. The proximity of the linear correlation coefficient, viz., R^2 to unity strongly aligns with the goodness of the fit. In this milieu, PSO models corresponded to 0.9916 and 0.9849 for

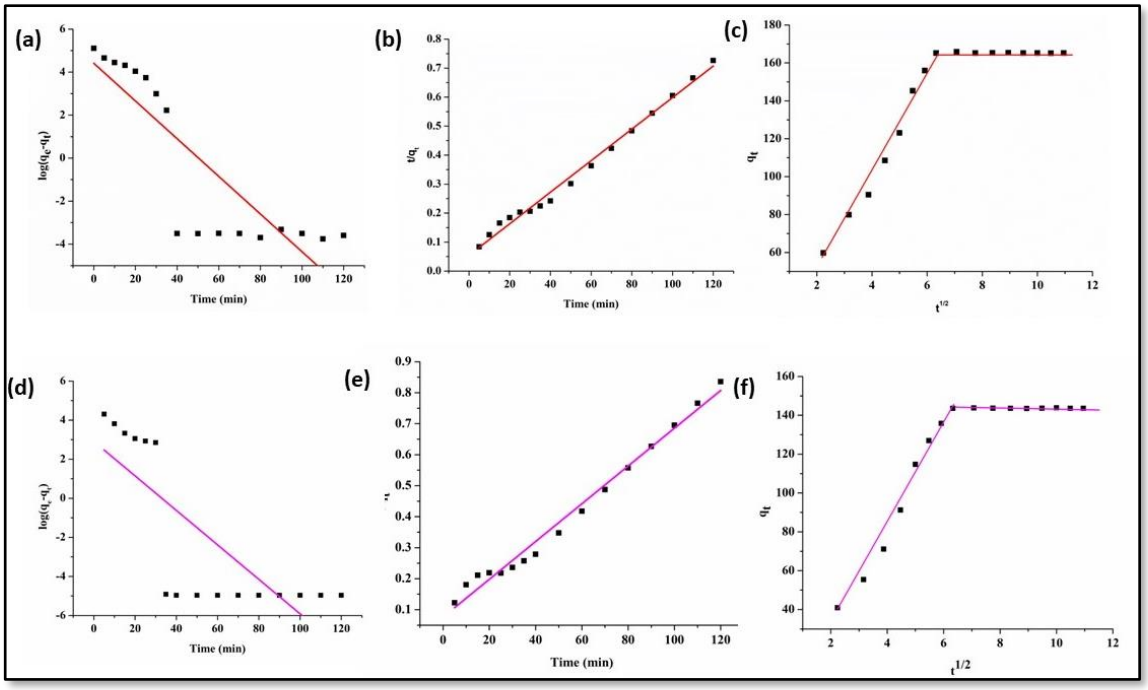

Figure 4.16. (a) PFO kinetics model, **(b)** PSO kinetics model, and **(c)** IPD model for MG dye, and **(d)** PFO kinetics model, **(e)** PSO kinetics model, and **(f)** IPD model for TZ dye.

MG and TZ dyes, respectively. Contrastingly, in the case of PFO, the linear correlation coefficients for MG and TZ were found to be 0.7270 and 0.5918, respectively. The correlation coefficient values indicated that the PSO is more reliable, suggestive of the fact that the chemisorption process occurs via ionic interactions between the adsorbent and adsorbate, with this step being the rate-determining step. The outcomes derived from various kinetic models are summarized in **Table 4.6.** In addition, the kinetics data were subjected to various analysis using the IPD model. As per the criteria of this model, a larger intercept, i.e., c signifies a greater boundary layer or thickness. Additionally, in the case where this process is involved in the adsorption mechanism, the plot of q_t against $t_{1/2}$ should exhibit a linear relationship. If this adsorption process plays a significant role in the rate ascertaining step, then the plot should pass through the origin. However, the presence of the multilinear plots indicates that more than one process operates simultaneously during the adsorption process [38-40].

Table 4.6. The kinetics variables for adsorption of MG and TZ on polymer nanocomposites.

Model	Kinetics parameters	MG	TZ
PFO	k_1	20.18×10^{-2}	20.32×10^{-2}
	R^2	0.72	0.59
PSO	k_2	5.4×10^{-3}	6.1×10^{-3}
	R^2	0.99	0.98
IPD	k_{ip}	7.83	3.18
	c	34.20	32.10
	R^2	0.71	0.69

4.4.0. Isotherm study

The adsorption isotherm elucidates the interactions existing between the adsorbate as well as the adsorbent molecules. The adsorption mechanism of dyes is assessed using the Langmuir, Freundlich and Temkin adsorption isotherms, as depicted in **Figure 4.17.** The mathematical forms for Langmuir, Freundlich and Temkin adsorption isotherms are represented by equations **4.6**, **4.7** and **4.8**, respectively. The results obtained from the

slopes and intercepts of the linear plots for Freundlich (ln q_e against ln C_e), Langmuir (C_e/q_e against C_e), and Temkin (q_e against ln Ce) are tabulated in **Table 4.7.** The data exhibited a poor fit with the Freundlich as well as Temkin model, thereby suggesting

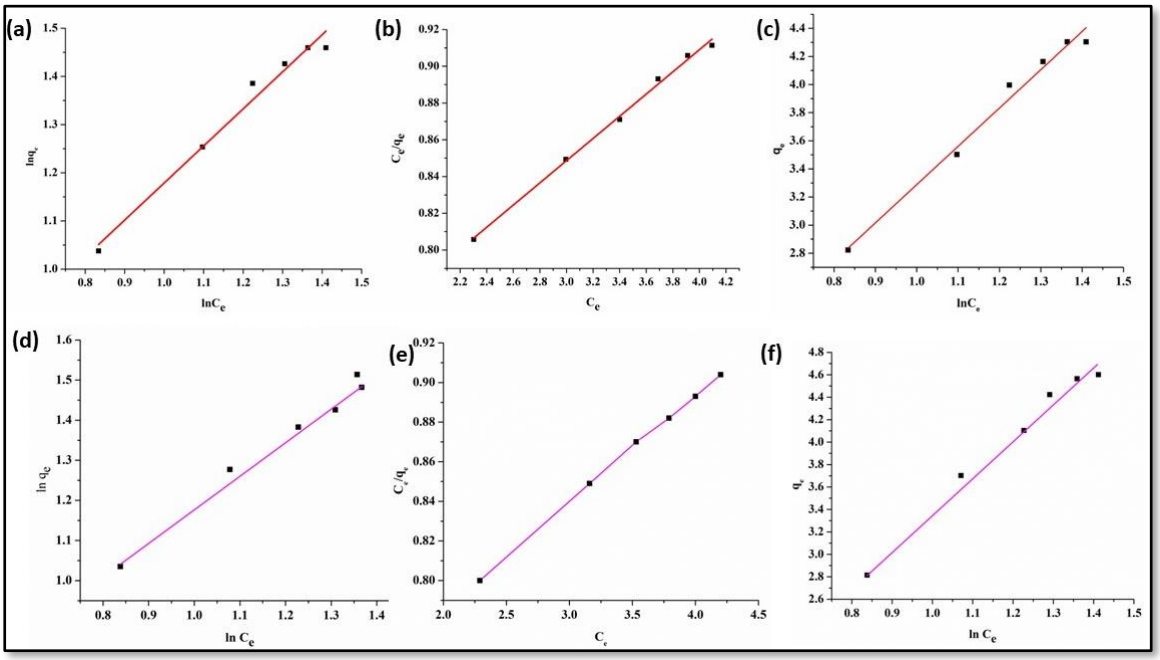

Figure 4.17. (a) Freundlich isotherm, **(b)** Langmuir isotherm, **(c)** Temkin isotherm for MG dye, and **(d)** Freundlich isotherm, **(e)** Langmuir isotherm, and **(f)** Temkin isotherm for TZ dye.

monolayer adsorption during the dye uptake process for both MG and TZ dyes. In contrast, the data aligned very well with the Langmuir adsorption isotherm, showcasing a high correlation factor, viz., 0.99 for both the dyes, viz., MG and TZ. This implied that the adsorption of MG and TZ dyes onto the mesoporous structure of the biochar material involved uniform binding energies with active sites distributed evenly across the surface of the adsorbents. Furthermore, this process of adsorption invokes physical adsorption across the layers of the polymer nanocomposites which are monolayer by nature. These findings strongly align with reports stated earlier [42]. Overall, the aforementioned findings concluded that Langmuir isotherm is the best fit for evaluating the dye adsorption study for both MG as well as TZ dyes.

4.4.1 Regeneration of adsorbent

To assess the recyclability of the adsorbent material for MG and TZ dye adsorption, the polymer nanocomposites were recovered through a simple procedure which involved filtration, followed by washing the contents thoroughly with deionized water and ethanol

[36]. Subsequently, the recovered samples of the polymer nanocomposites were dried at 105-110 °C. This recovery method was repeated seven times for conducting successive adsorption experiments. The results, as demonstrated in **Figure 4.18.**, indicate a promising recovering ability.

Table 4.7. The isotherm parameters for adsorption of MG and TZ on polymer nanocomposites.

Model	Isotherm variables	MG	TZ
Freundlich isotherm	n	2.07	2.81
	k_f	11.70	25.12
	R^2	0.97	0.95
Langmuir isotherm	Q_m	87.48	54.67
	k_l	0.22	0.28
	R^2	0.99	0.99
Temkin isotherm	b	3.21	4.50
	k_m	27.08	37.89
	R^2	0.98	0.97

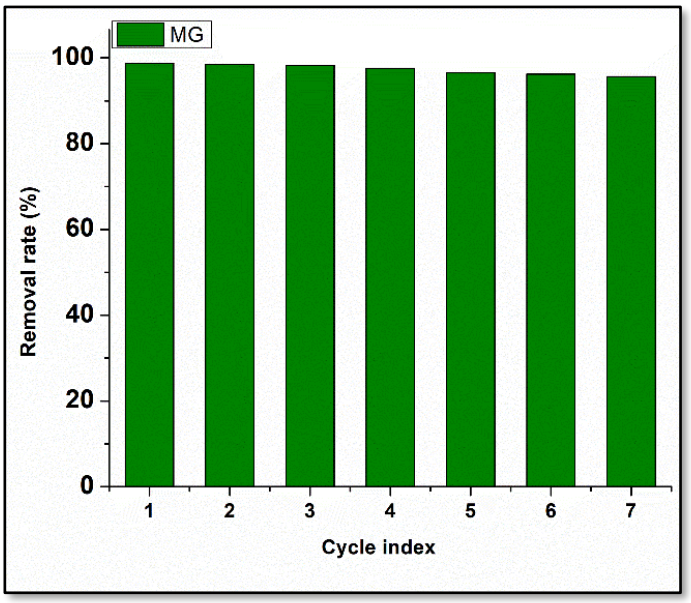

Figure 4.18. Removal rate for MG dye throughout seven consecutive cycles of reuse.

4.4.2. Conclusion

From an overall comprehensive study, it can be stated that an economically viable, efficient, and environmentally friendly adsorbent material, viz., biochar can be successfully synthesized from kraft lignin. The synthesized biochar was authenticated invoking various methods, viz., XRD, FTIR, Raman, XPS, etc. and was subsequently employed as a reinforcing agent in poly(ester amide urethane) resin in various loadings to carry out the fabrication of polymer nanocomposites. These nanocomposites demonstrated improved mechanical as well as thermal properties compared to the pristine polymer matrices along with rendering biodegradability attributes. In turn, they were successfully deployed as adsorbent material for removing MG and TZ dyes from aqueous systems with the excellent removal efficiency. An elaborate kinetics analysis proposed PSO kinetic model as the best fit for TZ and MG dye removal onto the polymer nanocomposites. Furthermore, Langmuir adsorption isotherm stood out as the best fit model for assessing the sorption traits of the polymer nanocomposites. Overall, the polymer nanocomposites exhibited excellent sustainability with satisfactory recovering ability as well as economic feasibility.

References

[1] Väisänen, T., Haapala, A., Lappalainen, R., and Tomppo, L. Utilization of agricultural and forest industry waste and residues in natural fiber-polymer composites: A review. *Waste management*, 54:62-73, 2016.

[2] Lawal, A. A., Hassan, M. A., Farid, M. A. A., Yasim-Anuar, T. A. T., Yusoff, M. Z. M., Zakaria, M. R., Roslan, A. M., Mokhtar, M. N., and Shirai, Y. One-step steam pyrolysis for the production of mesoporous biochar from oil palm frond to effectively remove phenol in facultatively treated palm oil mill effluent. *Environmental Technology & Innovation*, 18:100730, 2020.

[3] Wang, B., Gao, B., and Fang, J. Recent advances in engineered biochar productions and applications. *Critical Reviews in Environmental Science and Technology*, 47(22):2158-2207, 2017.

[4] Wang, J., Li, H., Liu, R., Li, L., Lin, Y. H., and Nan, C. W. Thermoelectric and mechanical properties of PLA/$Bi_{0.5}Sb_{1.5}Te_3$ composite wires used for 3D printing. *Composites Science and Technology*, 157:1-9, 2018.

[5] Giorcelli, M., Khan, A., Pugno, N. M., Rosso, C. and Tagliaferro, A. Biochar as a cheap and environmentally friendly filler able to improve polymer mechanical properties. *Biomass and Bioenergy*, 120:219-223, 2019.

[6] Yasim-Anuar, T. A. T., Ariffin, H., Norrrahim, M. N. F., Hassan, M. A., Tsukegi, T., and Nishida, H. Sustainable one-pot process for the production of cellulose nanofiber and polyethylene/cellulose nanofiber composites. *Journal of Cleaner Production*, 207:590-599, 2019.

[7] Essabir, H., Bensalah, M. O., Rodrigue, D., Bouhfid, R., and Qaiss, A. Structural, mechanical and thermal properties of bio-based hybrid composites from waste coir residues: Fibers and shell particles. *Mechanics of Materials*, 93:134-144, 2016.

[8] Nagarajan, V., Mohanty, A. K., and Misra, M. Biocomposites with size-fractionated biocarbon: Influence of the microstructure on macroscopic properties. *ACS Omega*, 1(4):636-647, 2016.

[9] Das, O., Bhattacharyya, D., Hui, D., and Lau, K. T. Mechanical and flammability characterizations of biochar/polypropylene bio-composites. *Composites Part B: Engineering*, 106:120-128, 2016.

[10] Khan, A., Savi, P., Quaranta, S., Rovere, M., Giorcelli, M., Tagliaferro, A., Rosso, C., and Jia, C. Q. Low-cost carbon fillers to improve mechanical properties and conductivity of epoxy composites. *Polymers*, 9(12):642, 2017.

[11] Poulose, A. M., Elnour, A. Y., Anis, A., Shaikh, H., Al-Zahrani, S. M., George, J., Al-Wabel, M. I., Usman, A. R., Ok, Y. S., Tsang, D. C., and Sarmah, A. K. Date palm biochar-polymer composites: An investigation of electrical, mechanical, thermal and rheological characteristics. *Science of the Total Environment*, 619:311-318, 2018.

[12] Ahmad, M., Rajapaksha, A. U., Lim, J. E., Zhang, M., Bolan, N., Mohan, D., Vithanage, M., Lee, S. S., and Ok, Y. S. Biochar as a sorbent for contaminant management in soil and water: a review. *Chemosphere*, 99:19-33, 2014.

[13] Kar, A. and Karak, N. Bio-based poly (ester amide): mechanical, thermal and biodegradable behaviors. *Journal of Polymer Research*, 29(9):366, 2022.

[14] Liu, X. J., Li, M. F., and Singh, S. K. Manganese-modified lignin biochar as adsorbent for removal of methylene blue. *Journal of Materials Research and Technology*, 12:1434-1445, 2021.

[15] Kar, A., Rather, M. A., Mandal, M., and Karak, N. Elastomeric biodegradable poly (ester amide urethane) as a tough and robust material. *Progress in Organic Coatings*, 182:107684, 2023.

[16] Hooi, K. K., Alimuddin, Z., and Ong, L. K. Laboratory-scale pyrolysis of oil palm pressed fruit fibres. *Journal of Oil Palm Research*, 21(1):577-587, 2009.

[17] Cantrell, K. B., Hunt, P. G., Uchimiya, M., Novak, J. M., and Ro, K. S. Impact of pyrolysis temperature and manure source on physicochemical characteristics of biochar. *Bioresource Technology*, 107:419-428, 2012.

[18] Idris, J., Shirai, Y., Andou, Y., Ali, A. A. M., Othman, M. R., Ibrahim, I., and Hassan, M. A. Self-sustained carbonization of oil palm biomass produced an acceptable heating value charcoal with low gaseous emission. *Journal of Cleaner Production*, 89:257-261, 2015.

[19] Huang, Y., Li, F., Meng, J., and Chen, W. Lignin content of agro-forestry biomass negatively affects the resultant biochar pH. *Bio Resources*, 13(3):5153-5163, 2018.

[20] Kumar, M., Verma, B. B., and Gupta, R. C. Mechanical properties of acacia and eucalyptus wood chars. *Energy Sources*, 21(8):675-685, 1999.

[21] Tanger, P., Field, J. L., Jahn, C. E., DeFoort, M. W., and Leach, J. E. Biomass for thermochemical conversion: targets and challenges. *Frontiers in Plant Science*, 4:218, 2013.

[22] You, S., Ok, Y. S., Chen, S. S., Tsang, D. C., Kwon, E. E., Lee, J., and Wang, C. H. A critical review on sustainable biochar system through gasification: Energy and environmental applications. *Bioresource Technology*, 246:242-253, 2017.

[23] Ahmed, M. J. and Hameed, B. H. Adsorption behavior of salicylic acid on biochar as derived from the thermal pyrolysis of barley straws. *Journal of Cleaner Production*, 195:1162-1169, 2018.

[24] Domingues, R. R., Trugilho, P. F., Silva, C. A., Melo, I. C. N. D., Melo, L. C., Magriotis, Z. M., and Sanchez-Monedero, M. A. Properties of biochar derived from wood and high-nutrient biomasses with the aim of agronomic and environmental benefits. *PloS One*, 12(5):0176884, 2017.

[25] Wang, W., Wang, C., Wang, T., Li, W., Chen, L., Zou, R., Zheng, J., and Li, X. Enhancing the thermal conductivity of n-eicosane/silica phase change materials by reduced graphene oxide. *Materials Chemistry and Physics*, 147(3):701-706, 2014.

[26] Zhang, Q., Yi, W., Li, Z., Wang, L., and Cai, H. Mechanical properties of rice husk biochar reinforced high density polyethylene composites. *Polymers*, 10(3):286, 2018.

[27] Mohammed, Z., Jeelani, S., and Rangari, V. Effective reinforcement of engineered sustainable biochar carbon for 3D printed polypropylene biocomposites. *Composites Part C: Open Access*, 7:100221, 2022.

[28] Jeon, J., Park, J. H., Wi, S., Yang, S., Ok, Y. S., and Kim, S. Characterization of biocomposite using coconut oil impregnated biochar as latent heat storage insulation. *Chemosphere*, 236:124269, 2019.

[29] Xu, J., Liu, J., Ling, P., Zhang, X., Xu, K., He, L., Wang, Y., Su, S., Hu, S., and Xiang, J. Raman spectroscopy of biochar from the pyrolysis of three typical Chinese biomasses: A novel method for rapidly evaluating the biochar property. *Energy*, 202:117644, 2020.

[30] Zhao, S. X., Ta, N., and Wang, X. D. Effect of temperature on the structural and physicochemical properties of biochar with apple tree branches as feedstock material. *Energies*, 10(9):1293, 2017.

[31] Nair, R. R., Mondal, M. M., Srinivasan, S. V. and Weichgrebe, D. Biochar synthesis from mineral-and ash-rich waste biomass, part 1: Investigation of thermal decomposition mechanism during slow pyrolysis. *Materials*, 15(12):4130, 2022.

[32] Lee, T., Nam, I. H., Jung, S., Park, Y. K. and Kwon, E. E. Synthesis of nickel/biochar composite from pyrolysis of Microcystis aeruginosa and its practical use for syngas production. *Bioresource Technology*, 300:122712, 2020.

[33] Ahmetli, G., Kocaman, S., Ozaytekin, I. and Bozkurt, P. Epoxy composites based on inexpensive char filler obtained from plastic waste and natural resources. *Polymer Composites*, 34(4):500-509, 2013.

[34] Idrees, M., Jeelani, S., and Rangari, V. Three-dimensional-printed sustainable biochar-recycled PET composites. *ACS Sustainable Chemistry & Engineering*, 6(11):13940-13948, 2018.

[35] Li, S., Huang, A. N., Chen, Y. J., Li, D., and Turng, L. S. Highly filled biochar/ultra-high molecular weight polyethylene/linear low density polyethylene composites for high-performance electromagnetic interference shielding. *Composites Part B: Engineering*, 153:277-284, 2018.

[36] Nan, N., DeVallance, D. B., Xie, X., and Wang, J. The effect of bio-carbon addition on the electrical, mechanical, and thermal properties of polyvinyl alcohol/biochar composites. *Journal of Composite Materials*, 50(9):1161-1168, 2016.

[37] Naghdi, M., Taheran, M., Brar, S. K., Rouissi, T., Verma, M., Surampalli, R. Y., and Valero, J. R. A green method for production of nanobiochar by ball milling-optimization and characterization. *Journal of Cleaner Production*, 164:1394-1405, 2017.

[38] Chaukura, N., Murimba, E. C. and Gwenzi, W. Sorptive removal of methylene blue from simulated wastewater using biochars derived from pulp and paper sludge. *Environmental Technology & Innovation*, 8:132-140, 2017.

[39] Naushad, M., Alqadami, A. A., AlOthman, Z. A., Alsohaimi, I. H., Algamdi, M. S., and Aldawsari, A. M. Adsorption kinetics, isotherm and reusability studies for the removal of cationic dye from aqueous medium using arginine modified activated carbon. *Journal of Molecular Liquids*, 293:111442, 2019.

[40] Claoston, N., Samsuri, A. W., Ahmad Husni, M. H., and Mohd Amran, M. S. Effects of pyrolysis temperature on the physicochemical properties of empty fruit bunch and rice husk biochars. *Waste Management & Research*, 32(4):331-339, 2014.

[41] Das, O., Kim, N. K., Hedenqvist, M. S., Lin, R. J., Sarmah, A. K., and Bhattacharyya, D. An attempt to find a suitable biomass for biochar-based polypropylene biocomposites. *Environmental Management*, 62:403-413, 2018.

[42] Zhang, Y., Fan, R., Zhang, Q., Chen, Y., Sharifi, O., Leszczynska, D., Zhang, R., and Dai, Q. Synthesis of $CaWO_4$-biochar nanocomposites for organic dye removal. *Materials Research Bulletin*, 110:169-173, 2019.

[43] Gu, Y., Xue, Y., and Zhang, D. Preparation of magnetic biochar with different magnetization sequences for efficient removal of oxytetracycline from aqueous solution. *Colloids and Surfaces A: Physicochemical and Engineering Aspects*, 626:126987, 2021.